Unravelling the origins and P-T-t evolution of the allochthonous Sobrado unit (Órdenes complex, NW Iberia) using combined U-Pb titanite, monazite and zircon geochronology and REE geochemistry

José Manuel Benítez-Pérez[1,3], Pedro Castiñeiras[2], Juan Gómez-Barreiro[3 (*)], José R. Martínez Catalán[3], Andrew Kylander-Clark[4], Robert Holdsworth[5]

[1]Centro de Ciências e Tecnologias Nucleares. Instituto Superior Técnico. Universidad de Lisboa. Estrada Nacional 10 (km 139,7), 2695-066, Bobadela LRS, Portugal
[2]Departamento de Mineralogía y Petrología. Facultad de Ciencias Geológicas, Universidad Complutense de Madrid. C/ José Antonio Novais, 12. Ciudad Universitaria, 28040, Madrid, Spain
[3]Departamento de Geología, Universidad de Salamanca, Pza. de los Caídos s/n, 37008, Salamanca, Spain
[4]Department of Earth Science, University of California, Santa Barbara, CA 93106, United States
[5]Earth Science Department, Durham University, Science Labs, Durham DH1 3LE, United Kingdom

Correspondence to: J. Gómez Barreiro (jugb@usal.es)

jose.benitez@ctn.tecnico.ulisboa.pt
castigar@ucm.es
jrmc@usal.es
kylander@geol.ucsb.edu
r.e.holdsworth@durham.ac.uk

Abstract

The Sobrado unit, within the upper part of the Órdenes complex (NW Iberia) represents an allochthonous tectonic slice of exhumed high grade metamorphic rocks formed during a complex sequence of orogenic processes in the middle to lower crust. In order to constrain those processes, U-Pb geochronology and REE analyses of accessory minerals in migmatitic paragneisses (monazite, zircon), and mylonitic amphibolites (titanite) were conducted using LASS-ICP-MS. The youngest metamorphic zircon age obtained coincides with a Middle Devonian concordia monazite age (~380 Ma) and is interpreted to represent the minimum age of the Sobrado high-P granulite-facies metamorphism that occurred during the early stages of the Variscan Orogeny. Metamorphic titanites from the mylonitic amphibolites yield a Late Devonian age (~365 Ma) and track the progressive exhumation of the Sobrado unit. In zircon, cathodoluminescence images and REE analyses allow two aliquots with different origins in the paragneiss to be distinguished. An Early Ordovician age (~490 Ma) was obtained for metamorphic zircons, although with a large dispersion, related to the evolution of the rock. This age is considered to mark the onset of granulite-facies metamorphism in the Sobrado unit under intermediate-P conditions, and related to intrusive magmatism and coeval burial in a magmatic arc setting. A maximum depositional age for the Sobrado unit is established in the late Cambrian (~511 Ma). The zircon dataset also record several inherited populations. The youngest cogenetic set of zircons yields crystallization ages of 546 and 526 Ma and are thought to be related to the peri-Gondwana magmatic arc. The additional presence of inherited zircons older than 1000 Ma is interpreted as suggesting a West African Craton provenance.

Keywords: U-Pb geochronology, LASS-ICP, zircon, titanite, monazite, REE, Sobrado Unit

1. Introduction

Zircon, monazite and titanite are accessory mineral phases found in rocks with a very wide range of compositions. These minerals can resist numerous sedimentary, igneous and metamorphic events across a wide range of temperatures, pressures and strains, even when fluids are present. Frequently, compositional domains can be defined in these minerals that record changes in different parameters (Storey et al., 2007; Castiñeiras et al., 2010; Stübner et al., 2014; Hacker et al., 2015; Stearns et al., 2016; Stipska et al., 2016). These minerals additionally provide several closed decay chains or disintegration systems ($^{238}U \rightarrow {}^{206}Pb$, $^{235}U \rightarrow {}^{207}Pb$ y $^{232}Th \rightarrow {}^{208}Pb$), because they hold variable concentrations of uranium (U) and/or thorium (Th) in their crystal lattices. Such variations in concentration allow accurate dating using microscopic scale analysis (tens of microns size).

Titanite is stable in metabasites across a wide range of metamorphic conditions (Spear, 1981; Frost et al., 2000) and is able to record metamorphic and deformational events (Franz and Spear, 1985; Verts and Frost, 1996; Rubatto and Hermann, 2001; Spencer et al., 2013; Stearns et al., 2015, 2016). The titanite U/Pb system is a widely used geochronometer for deformation events in granulite-amphibolite facies rocks (Spear, 1981; Cherniak, 2006; Harlov et al., 2006). Monazite is common in amphibolite and higher-grade facies. Zoning in this mineral can have an igneous or metamorphic origin (DeWolf et al., 1993; Hawkins and Bowring, 1997; Zhu et al., 1997; Spear and Pyle, 2002). The crystallization stages seen in zoned monazites, with changes in Y, Ca, Si, Sr, Ba, REE, U and Th, has been linked to certain metamorphic reactions (Kohn and Malloy, 2004; Corrie and Kohn, 2008) or deformation process (Terry and Hamilton, 2000). Zircon survives the majority of magmatic, metamorphic and erosive terrestrial processes. Cathodoluminescence analysis of zircon zoning patterns allows a large variety of reactions to be distinguished and can clarify the petrogenetic evolution (Corfu et al., 2003). Th/U ratios can also be used to separate zircon based on their igneous or metamorphic origin (Hoskin and Ireland, 2000; Möller et al., 2002; Hokada and Harley, 2004; Hoskin, 2005). Rare-earth element (REE) abundances can also be used as a qualitative petrological indicator. Heavy rare-earth elements (HREE) are preferentially incorporated into zircon compared to light rare-earth elements (LREE). Hence, the normalized HREE slope can be used to interpret whether a zircon crystallized or recrystallized when garnet and xenotime (YPO_4) were present, because these minerals also preferentially assimilate HREE in the lattice (Hoskin and Ireland, 2000; Rubatto, 2002; Hermann and Rubatto, 2003; Rubatto et al., 2009).

The events recorded in individual grains can be radiometrically dated employing combined laser ablation analyses and cathodoluminescence (CL) images in zircons (Corfu et al., 2003) and compositional maps obtained using electron microprobe (EMPA) in monazite (Gonçalves et al., 2005; Williams et al., 2007) to recognize different growth zones. The chemical analysis, especially REE, links the development of growth zones to specific metamorphic or deformative events (Frost et al., 2000; Rubatto, 2002; Whitehouse and Platt, 2003; Zheng et al., 2007; Chen et al., 2010; Gagnevin and Daly, 2010; Holder et al., 2015;). Simultaneous geochronology and REE data are a powerful tool in the interpretation of ages - this is known as REE-assisted geochronology (Castiñeiras et al., 2010).

This methodology has been applied to selected samples of the Sobrado unit (Fig. 1), which forms part of the allochthonous complexes of NW Iberia and one where the structural and metamorphic evolution is rather well known (Pablo Maciá et al., 1984; Díaz García et al., 1999; Arenas and Martínez Catalán, 2002; Benítez-Pérez, 2017). This unit occurs in the Upper Allochthon of the Órdenes complex, and represents a tectonic slice of exhumed ultramafics, eclogites, high-P granulites, amphibolites and migmatitic paragneisses derived from a peri-Gondwanan terrane. It evolved along a complex sequence of geological processes involving Cambro-Ordovician rifting with voluminous bimodal plutonism, nearly contemporaneous granulite facies metamorphism of intermediate-P, early Variscan subduction and subsequent exhumation by ductile thrusting during Variscan collision with the external margin of northern Gondwana.

Previous geochronological data on the Sobrado unit include U-Pb ages from four samples (Fernández-Suárez et al., 2002, 2007). A middle Cambrian protolith age of a gabbro and a Middle Devonian metamorphic age of a high-P basic granulite supposedly derived from the same gabbro were obtained by zircon dating. Zircon in a migmatitic, mylonitized paragneisses yielded discordant ages with an Early Ordovician lower intercept, while monazite dating provided Cambro-Ordovician ages in another migmatitic, mylonitized paragneiss. This new study aims at constraining the metamorphic evolution of the unit including dating a migmatitic paragneiss, as previous data missed the early Variscan ages found in intercalated high-P granulites, and also an amphibolite, which could date advanced stages of exhumation. Monazite and zircon ages of paragneisses and titanite ages of amphibolites taken from separate, but presently adjacent tectonic slices of the high-P/high-T of Sobrado unit are compared and interpreted using REE-assisted geochronology. This sheds new light upon the possible origin, ages and relationships between the regional foliation development and the partial melting processes that have occurred in this and equivalent units of the NW Iberia Upper Allochthon.

2. Geological background

The Allochthonous complexes in NW Iberia are remmants of a huge nappe stack preserved as klippen in the core of late Variscan synforms. They consist of units mostly of peri-Gondwanan derivation, which can be classified in three groups based on their structural position in the tectonic pile and origin: The Upper, Middle and Lower allochthons (Fig. 1).

The Upper Allochthon is a piece of the northern margin of Gondwana detached and drifted away during the Cambro-Ordovician opening of the Rheic Ocean. The Middle Allochthon is formed by lithospheric pieces of oceanic affinity, or oceanic supracrustal sequences that formed part of the Rheic oceanic realm and are often referred to as ophiolitic units. The Lower Allochthon derives from distal parts of the Gondwanan continental margin.

The Allochthon units are separated from the Iberian Autochthon by a series of kilometer-scale imbricated sheets, known as the Parautochthon (Ribeiro et al., 1990), or Schistose Domain in Galicia (NW Spain), consisting of a set of Paleozoic metasedimentary and volcanic rocks. The Parautochthon has stratigraphic and igneous affinities with the Iberian autochthon of the Central Iberian Zone, and no ophiolites occur between them. For these reasons it is interpreted as a distal part of the Gondwanan continental margin (Farias et al., 1987; Dias da Silva et al., 2014).

The allochthonous units are regarded as a stack of Varican thrust sheets with associated tectonic fabrics and metamorphic events. Due to the "piggy-back" nature of the sequence, the structurally higher units are thought to represent the furthest travelled paleogeographic domains. Recumbent folds, thrusts and extensional detachments formed during the Variscan collision are found in all three allochthonous units (Martínez Catalán et al., 1999; Gómez-Barreiro et al., 2007).

Maximum sedimentation ages obtained from the study of detrital zircon carried out in metasediments from the Upper allochthon can be estimated between 530 and 510 Ma (e.g., Fuenlabrada et al., 2010). Intrusive rocks in the Upper allochthon have been dated between 520 and 490 Ma and are associated with the development of a magmatic arc which evolves into an extensional scenario that ended with the opening of the Rheic ocean (Peucat et al., 1990; Ordóñez Casado, 1998; Abati et al., 1999, 2007; Fernández-Suárez et al., 2007; Castiñeiras et al., 2010). Two high-P/high-T metamorphic events have been recognized in this unit. The oldest one has yielded 490-480 Ma (Kuijper 1979; Peucat et al. 1990; Abati et al., 1999, 2007; Fernández-Suárez et al., 2002) and the youngest one has been dated approximately between 405-390 Ma (Santos Zalduegui et al., 1996; Ordóñez Casado et al., 2001; Fernández-Suárez et al., 2007). In the Middle allochthon, crystallization ages vary between 390 and 375 Ma (Peucat et al., 1990; Dallmeyer et al., 1991, 1997) and ages from 375 to 365 Ma have been related to continental subduction (Santos Zalduegui et al., 1995; Abati et al., 2010). Thrust wedge collapse, in the middle and lower allochthonous units, is thought to have happened between 390 and 365 Ma, followed by a collision in the internal zones around 365-330 Ma, causing further folding and thrusts (Dallmeyer et al., 1997; Martínez Catalán et al., 2009). Afterwards, there was another extensional collapse phase until 315 Ma, followed by a final phase of shortening and folding up until approximately 305 Ma related to the regional oroclinal bending in Iberia (Aerden, 2004; Martínez Catalán, 2011, 2012; Álvarez-Valero et al., 2014).

The Upper Allochthon is further subdivided into high-P/high-T and intermediate-P units (Gómez Barreiro et al., 2007). The present study focuses on two of the high-P/high T upper units (Figs. 1 and 2). The origin of the high-P event recorded in these units is controversial, but might reflect the accretion of the units into the continental part of northern Gondwana, during the Early-Middle Devonian (400-390 Ma; Ballèvre et al., 2014).

The Sobrado antiform consists of three tectonic slices bounded by two extensional detachments (Figs. 1 and 2). The lower tectonic slice comprises highly serpentinized ultramafic rocks with interlayered metabasite units. The metabasites include eclogites (Omp + Grt + Qtz + Rt ± Ky and Zo, mineral abbreviations according to Whitney and Evans, 2010) and related clinopyroxene-garnet rocks without primary plagioclase (Cpx + Grt + Qtz + Rt ± Zo), as well as other types of rocks derived from the retrogression and mylonitization of the early high-P stages. The intermediate tectonic slice is made up of migmatitic felsic gneisses (mainly paragneisses), with frequent inclusions of high-P granulites (Cpx + Grt + Pl + Qtz + Rt ± Ky). Remnants of igneous protoliths are not preserved either in the lower or intermediate tectonic slices. The upper tectonic slice, however, contains migmatitic felsic gneisses and mafic layers derived from deformed and recrystallized gabbros with locally preserved relict igneous textures, reaching high-P granulite facies conditions. The progressive transformation from gabbros to high-P granulites (Na-Di + Grt + Pl + Qtz + Rt) has occurred in a series of different stages with a metamorphic peak at 13-17 kbar and 660-770ºC (Arenas and Martínez Catalán, 2002).

The metamorphic evolution of the Sobrado Unit as described in the literature indicates that felsic gneisses underwent differing degrees of partial melting after the metabasites reached their peak pressure. Consequently, the felsic gneisses are thought to have developed a regional foliation under amphibolite facies conditions, as did the amphibolic gneisses, "flaser" amphibolites, and fine-grained amphibolites. This metamorphic evolution is described by Arenas and Martínez Catalán (2002) as a clockwise P-T path, with a metamorphic peak of, at least, 15 kbar and >800ºC, followed by an isothermal decompression. This trajectory is interpreted to result from gravitational collapse of an overthickened orogenic wedge (Gómez-Barreiro et al., 2007; Ballèvre et al., 2014). Although some regional structures, such as the Fornás detachment (FD, Fig. 1; Gómez-Barreiro et al., 2007; Álvarez-Valero et al., 2014) or the Corredoiras detachment (CD, Fig. 1; Díaz García et al., 1999), have been related to this gravitational readjustment, no study has dealt with the development of the extensional fabrics in any detail. Overall, it is thought that the extensional flow has generated a pervasive thinning of the orogenic pile and that the preserved sequence of tectonic slices is strongly condensed.

3. Sample description and Methodology

3.1. Selected samples

Two representative samples (*JBP-71-15A* and *JBP-71-21*) were selected from two structurally separate but currently adjacent parts of the high-P/high-T Sobrado unit, within the Órdenes complex, for laser ablation (LASS-Laser Ablation Split Stream) analyses, including U–Pb geochronology and REE determinations. The samples locations are presented in Figure 2.

Sample *JBP-71-21* is a mylonitic fine-grained amphibolite, without any preserved igneous relicts. Fine-grained amphibolites represent an advanced stage in the mylonitization of the metabasites. They appear as relatively thin layers inside the maffic rocks and dominate in a thick mylonitic layer (300

- 700m; Fig. 2; Arenas and Martínez Catalán, 2002; Benítez Pérez, 2017) located at the base of the upper tectonic slice. The sample comprises Hbl + Pl + Grt ± Cpx + Bt ± Rt ± Ttn ± Ilm ± Zo ± Qtz (Fig. 3). Mylonitic foliation and lineation are defined by amphibole and plagioclase (Fig. 3). Garnet appears as subrounded porphyroclasts partially resorbed (Fig. 3). Titanite grains are parallel to the foliation and in textural equilibrium with plagioclase and amphibole. Rutile and ilmentite are always hosted as inclusions both in titanite and/or garnet (Fig. 3 c, d).

Sample *JBP-71-15A* is a granulite facies migmatitic paragneiss from the underlying intermediate tectonic slice. It comprises Qtz + Pl + Grt + Kfs + Ky + Bt + IIm + Rt and shows microscopic scale textural evidence of partial melting. Temperature and pressure estimation ranges between 750-850ºC and 11-16 kbar for the anatectic fabric (Benítez-Pérez, 2017). Leucocratic domains with Qtz, Kfs and Pl, with evidence of plastic deformation define the foliation and Bt, Ky, Rt and Grt define linear aggregates resulting in a pervasive lineation (Fig. 4). Along the strained leucosomes, garnets show evidence of plastic deformation (Benítez Pérez, 2017) like (Fig. 4 a, f, g): sigmoidal, dumb-bell-shaped grains and pinch-and-swell microstructures (Ji and Martignole, 1994; Kleinschrot and Duyster, 2002; Passchier and Trouw, 2005). Zircon and monazite are found in different microtextural settings. Small-elongated prims of zircon are always found shielded whithin garnets (Fig. 4 g), while relatively larger zircon grains with irregular, elongated, sub-rounded shapes, appear across the fabric in leucosomes, biotite aggregates and even within kyanite crystals (Fig. 4 a,b,c,d,f). In few cases, elongated/sub-rounded zircons have been found as inclusions in garnets (Fig. 4 e). Monazite grains show elongated to sub-rounded grains located in Qtz-Kfs-Pl-Bt domains, which define the main foliation of the rock (Fig. 4 d,f,h).

3.2. Sample preparation

Sample preparation was carried out at the laboratories of the Universidad Complutense (Madrid). The rocks were crushed, pulverized and sieved to achieve a 0.1-0.5 mm grain size. Heavy minerals were concentrated using a Wilfley™ table. The non-magnetic minerals from this heavy fraction are then separated using a Frantz isodynamic magnetic separator. A final concentrated fraction is obtained using heavy liquids (methylene iodide, CH_2I_2).

Zircon (translucent, colourless or light brown), monazite (yellow) and titanite (colorless) grains are selected by handpicking, according to their external morphology viewed under a binocular microscope. All the grains collected were arranged separately in parallel rows, mounted on glass slide with a double-sided adhesive and set in epoxy resin. After the resin was cured, the surface was eroded using a wet abrasive silicon carbide abrasive paper (4000 grit) and polished with 0.3 μm aluminium oxide. The surface was then coated with gold, to avoid charging problems under the scanning electron microscope (SEM). Prior to isotopic analysis, cathodoluminescence images (CL) of zircon grains were taken on a JEOL JSM-820 SEM, and compositional maps of monazite grains were created on a JEOL Superprobe JXA-8900M microprobe (National Center for Electron Microscopy, Madrid). Secondary electron images (SE) were also taken to determine the exact location of the spots, identify the internal structure, and presence of inclusions and defects in zircon, monazite and titanite grains.

3.3. Mineral description

Titanite grains are generally rounded, with an average grain size of 100 μm, and irregular morphologies. Their secondary electron images reveal homogeneous compositions and the presence of solid inclusions. This grain size permits large spatial resolution analyses (50 μm) to be carried out. Monazite grains have a more variable grain size distribution, with an average of 60-70 μm. Their habit is irregular and they usually show rounded morphologies or broken grains. We carried out La, Th, Y, U and Nd compositional maps for every monazite grain in order to discover a compositional zonation that could be attributed to different growth events. Thorium zoning is the one that developed better and was taken into account to select the spots for isotopic analysis (Fig. 5), yet it never exceeds 30% of the grain.

Several spots were analyzed in monazite crystals with the greatest compositional contrasts to determine if they really represented different growth stages in the monazite grains.

Zircon grains from the paragneisses usually have scarce mineral inclusions and they can display a wide variety of morphologies, including irregular and sub-rounded shapes typical of metamorphic zircon, pristine elongated dipyramidal prisms interpreted as igneous in origin, and equigranular grains with abrasion signs with a probable detrital origin. Their length-to-width ratios vary between 3:1 and 2:1. Cathodoluminescence images (Fig. 6) are useful to relate the crystallization of parts of zircon crystals to specific igneous, metamorphic or deformational events (Corfu et al., 2003, Nasdala et al., 2003, Zeck et al., 2004). It is common to image a homogeneous xenocrystic core in zircon grains and even a less luminescent mantle in some grains (grain numbers 5, 6). The core aspect is mainly rounded, with irregular or angular shapes. In most of the zircon grains, the internal parts of the grains display an oscillatory zoning (grain numbers 33, 71), with different thickness, although in some cases, this zoning is faint (grain number 26). There are several grains with sector zones (grain numbers 26, 27) parallel to the zircon *c*-axis (Watson and Yan Liang, 1995) and even one case of soccerball zoning (grain number 82). The zoning usually appears to be partially truncated and surrounded by a discontinuous poorly luminescent rim (grain numbers 20, 79).

3.4. Analytical techniques

U/Th-Pb, REE and Hf analyses of zircon, titanite and monazite were carried out using the laser ablation split stream (LASS) at the University of California at Santa Barbara (UCSB). The samples were ablated using a Photon Machines 193 nm ArF excimer ultraviolet laser with a HelEx ablation cell coupled to a Nu Instruments Plasma high-resolution multi-collector inductively coupled plasma mass spectrometer (MC-ICP-MS) and either a Nu Instruments AttoM high-resolution single-collector ICP or an Agilent 7700S quadrupole ICP-MS (Kylander-Clark et al., 2013). This installation allows the simultaneous isotopic and compositional (REE) analysis to be carried out. The laser spot diameter was 20 μm for zircon, 7-10 μm for monazite (Košler et al., 2001) and 50 μm for titanite (Stearns et al., 2016), resulting in pit depths between 6 μm for monazite and 30 μm for titanite. The laser has a fluence of ~1 J/cm^2 and was fired twice to remove common Pb from the sample surface. This material was allowed to wash out for 15 s, prior to the material being ablated at 3 Hz for 20 s for analysis. On the ICP-MS, the masses ^{204}Pb+Hg, ^{206}Pb, ^{207}Pb, and ^{208}Pb were measured using ion counters, and the masses ^{232}Th and ^{238}U were measured using Faraday detectors.

The U/Th-Pb standardization for monazite was carried out using sample 44069 (Aleinikoff et al., 2006) as the primary reference material (RM), whereas the Bananeira sample was employed as primary RM for trace element corrections (Kylander-Clark et al., 2013; Palin et al., 2013). Additionally, FC-1 (Horstwood et al., 2003), Trebilcock (Tomascak et al., 1996) and Bananeira were also used as secondary monazite RM, allowing ^{206}Pb/^{238}U ages to be within 2% of their accepted values. U-Pb proportions in titanite were corrected using Bear Laken (Aleinikoff et al., 2007) and Y1710C5 (Spencer et al., 2013) as RM. 91500 (Wieldenbeck et al., 1995) and GJI (Jackson et al., 2004) were used as RM for zircon, both for isotopic composition and trace element calibrations. Radiogenic lead versus common lead (^{207}Pb/^{206}Pb) measurements require up to 2% additional external error attributable either to variation count statistics, or ablation signal stability (Spencer et al., 2013; Hacker et al., 2015b). These external errors were incorporated into the data in the experiments.

The Iolite plug-in v. 2.5 (Paton et al., 2011) from the Wavemetrics Igor Pro software was used to improve and reduce the analyses (Hacker et al., 2015). The isotopic ratios ^{238}U/^{206}Pb and ^{207}Pb/^{206}Pb for each analysis were plotted on Tera-Wasserburg diagrams using Isoplot and Topsoil programs (Ludwig, 2012; Zeringue et al., 2014). All date uncertainties are reported at the 95% confidence interval, assuming a Gaussian distribution of measurement errors. Zircon, titanite, and monazite REE analyses were normalized against the McDonough and Sun (1995) chondrite values.

4. Results

4.1. Titanite (amphibolite, upper tectonic slice)

Fifty-one titanite analyses were projected onto a Tera-Wasserburg concordia plot (Fig. 7 a). After a preliminary evaluation, twelve analyses were rejected due to either high common Pb or high discordance (>10%) and were considered no further (Table 1). The remaining analyses define a Pb/U semi-total isochron between the common or initial Pb (^{207}Pb) and radiogenic Pb (^{206}Pb) (Ludwig, 1998). The good fit of the isochron confirms the chemical homogeneity of the data (Stearns et al., 2016) and it intercepts the concordia at 364.8 ± 4.5 Ma (2σ). Titanite chondrite-normalized REE analyses are detailed in Table 1 and are shown in Fig. 7 b. Titanite REE patterns are convex upwards, relatively flat, with slight LREE depletions versus HREE with respect to chondrite. They generally lack a europium anomaly (Eu*), but some analyses show a non-distinctive positive or negative anomaly.

4.2. Monazite (paragneiss, middle tectonic slice)

For monazite U/Th-Pb geochronology, we used the thorium zoning in monazite grains to select the analytic spots. As shown in Figure 5 there are no significant age differences between spots or zones with different Th chemical concentrations in a single grain. The obtained REE patterns are also very similar, and the mismatch at the HREE is probably due to either uncertainties in measurement because of the lower counts or interference effects of intermediate rare-earth oxides (Holder et al., 2015).

Data from seventy-six U/Th-Pb monazite analyses are shown in Table 2 and displayed using a Tera-Wasserburg concordia plot (Fig. 8 a). Four of these analyses, not related to chemical zoning, were discarded due to common Pb loss and were considered no further. The remaining analyses form a single population (mean square of weighted deviation; MSWD = 0.48) centered on a concordia age of 382.5 ± 1.0 Ma (2σ). Monazite geochemistry is shown in Figure 8b. REE patterns analyzed show an LREE enrichment, HREE depletion and negative Y anomalies with respect to chondrite with little variation within or between samples.

4.3. U-Pb zircon (paragneiss, middle tectonic slice)

Eighty-three analyses were performed on eighty zircon grains from the Sobrado paragneiss (Table 3). In a preliminary assessment of the data two analyses were rejected due to analytical errors (grain numbers 8, 36). Additionally, 23 analyses yielded a discordance higher than 10% and will not be further considered. The remaining 58 zircon analyses are shown on a Wetherill concordia plot (Fig. 9 a). The ^{207}Pb/^{206}Pb ages older than 1000 Ma are presented in a probability density plot (Fig. 9b). Most of the old ages are distributed between 1880 and 2200 Ma, with two peaks at 2030 and 2100 Ma. Three ages are older, around 2600 Ma, and there are also two analyses around 1300 Ma. The ^{206}Pb/^{238}U ages younger than 1000 Ma are ploted in a Tera-Wasserburg concordia plot (Fig. 10 a) and a probability density plot (Fig. 10 b). The data are continuously distributed between 589 and 380 Ma and attending to their CL texture, ages from 589 to 510 Ma are obtained mainly from internal areas with oscillatory or sector zoning (e.g., 33, 27 and 62, see Fig. 6); whereas, ages from 510 to 380 Ma correspond to discordant rims that have homogeneous CL signal, except for some grains (e.g., 10, 11 and 26, see Fig. 6) that are cores with oscillatory or sector zoning.

4.4. REE zircon (paragneiss, middle tectonic slice)

The chondrite-normalized REE patterns of the zircons with ages older than 600 Ma are shown in Figure 11. In general, this group has REE patterns with a pronounced fractionation from light to heavy REE and two anomalies in Ce (positive) and in Eu (negative). There are only three analyses that diverge from this trend and show a flat HREE pattern.

For the younger analyses, the chondrite-normalized REE patterns have different features depending on the age (Fig. 12). The oldest ages (589-510 Ma) show a tight HREE fractionation, variable Eu anomaly, and a pronounced Ce anomaly. The youngest ages (510-380 Ma) has a variable HREE slope, whereas the Eu anomaly is more regular, and the Ce anomaly is less marked.

When we plot age versus Hf, Yb/Gd and Eu/Ey* (Figs. 13 a, b, c), the group of oldest ages (589-510 Ma) does not define any apparent trend. In sharp contrast, in the 500-380 Ma group it is remarkable not only the good correlation between age and composition, but also the divergent evolution depending of the age (grey arrows). Hafnium, Yb/Gd and Eu/Eu* increase from 500 to ~430 Ma while there is a striking decrease from ~420 to 380 Ma. Finally, we have used the U/Ce-Th graph proposed by Bacon et al. (2012) to discriminate between metamorphic and igneous zircon.

5. Discussion

5.1. Zircon geochronology: inheritance and age of magmatism

The presence of zircon inclusions shielded in garnets (e.g. Fig. 4 e and g) is compatible with the preservation of magmatic, metamorphic or detrital inheritances during the synkinematic partial melting recorded in these rocks (Benítez Pérez, 2017). As shown in Fig 12, the majority of analyzed zircon grains older than 600 Ma have fractionated REE patterns that are characteristic of igneous zircon (Hoskin and Schaltegger, 2003, Whitehouse and Platt, 2003; Hanchar and Westrenen, 2007; Grimes et al., 2015). Only three analyses show a flat HREE pattern that can be related to the presence of garnet and interpreted as metamorphic zircon. The provenance of these zircon grains older than 600 Ma in the Sobrado migmatitic paragneisses (Fig. 9 b), is probably similar to those reported in the intermediate-P units of NW Iberia upper allochthons like the Betanzos unit (Fuenlabrada et al., 2010) and Cariño gneisses (Albert et al., 2015). We obtained two Mesoproterozoic ages, between 1.2 and 1.4 Ga. Similar ages are also found in the Parautochthonous (Díez Fernández et al., 2012), in the basal allochthonous units (Díez Fernández et al., 2010) and, to a lesser extent, in the intermediate-P units of NW Iberia (Albert et al., 2015). These inherited zircons, although scarce (Fernández-Suárez et al., 2003), likely have their origin in rocks derived from Saharan and Arabian-Nubian cratons, and presumably transported during the Cadomian orogeny (e.g., Martínez Catalán et al., 2004). Paleoproterozoic populations range from 1.8 to 2.2 Ga, clustered at 2.1 Ga, are also common in the Allochthonous complexes (Fernández-Suárez et al., 2003) and their origin likely involves materials generated or reworked during the Eburnian orogeny (e.g., Egal et al., 2002; Ennih and Liegeois, 2008) from the West African craton (Peucat et al., 2005). Finally, the Archean population in the Sobrado paragneisses ranges from 2.5 to 2.8 Ga, and it is likely related to intrusive events in the Western Reguibat Shield (Schofield et al., 2012) and the northern part of the West African craton (Albert et al., 2015), with some reworking processes of juvenile rocks formed at ca. 3.0 Ga (Potrel et al., 1998).

Based on CL images, ages and zircon composition, we can determine that the youngest zircon with magmatic origin is grain number 34 (Fig. 6). The number obtained in this grain is comparable to other maximum depositional ages obtained from similar units in the NW Iberia allochthonous complexes, such as the intermediate-P Betanzos uppermost unit (530-510 Ma, Fuenlabrada et al., 2010), and the intermediate-P Cariño uppermost unit (~510 Ma, Albert et al., 2015).

In order to get more insight into the meaning of the data younger than 600 Ma, we have plotted these ages versus the Th/U ratios (Fig. 14). Analyses that yielded ages between 589 and 510 Ma cluster together with Th/U values higher than 0.3. The REE patterns displayed in this cluster are consistent with a magmatic origin. In the age versus Hf, Yb/Gd and Eu/Eu* plots for this group (Fig. 13 a, b, c), the absence of a trend suggests that the different zircon grains are not connected by a fractional crystallization process (e.g., Barth and Wooden, 2010). In the U/Ce-Th graph proposed by Bacon et al. (2012) to discriminate between metamorphic and igneous zircon. In this diagram, zircon with ages between 589 and 510 Ma plot in the igneous zircon field (Fig. 13 d).

From the first group of data between 589 and 510 Ma, we can extract two ages, 546 ± 5 Ma out of six analyses, and 526 ± 3 Ma from 14 analyses (Fig. 15). These magmatic ages are also recognized in other well-characterized high-P/high-T units of the allochthonous complexes (Peucat et al., 1990; Santos Zalduegui et al., 2002; Castiñeiras et al., 2010), and they are related to a magmatic arc creation around the periphery of Gondwana (Abati et al., 1999, 2007).

5.2. Evolution of metamorphism of the Sobrado migmatitic paragneiss based on zircon composition

Extracting ages from a dataset where the data are evenly distributed from 500 to 380 Ma is a challenging task. When such smear in the age sorting happens, if we can rule out analytical error, we have three possibilities (e.g., Castiñeiras et al., 2010), namely, (i) the correct age is the youngest and the dispersion is related to zircon inheritance, (ii) the real age is the oldest and the spread is caused by lead loss, or, (iii) the age range is recording some kind of protracted geological event. Taking into account the CL texture of the youngest spots, we can remove the first possibility as the majority of analyses were performed in zircon rims. Furthermore, maximum depositional ages obtained from similar units from the Allochthonous complexes preclude their interpretation as inheritance. The second possibility is plausible, considering the complex metamorphic evolution and the high grade attained by these rocks. However, a young lead loss episode should have affected also the inherited zircon ages, and the presence of various old age peaks (e.g., ~2000, 546 and 536 Ma) suggests that they did not experienced lead loss. However, we can argue that limited lead loss occurred in some grains that have similar composition to the 589-510 Ma group (Th/U> 0.15), but younger ages (between 502 and 468 Ma). This group of outlier analyses (#10, 11, 26 and 63) could have experienced a decoupling between their actual age and their composition (e.g., Flowers et al., 2012). Finally, we favor the last option when we take into account the strong correlation observed between age and zircon composition (Figs. 13 a, b, c and 14).

This group of young analyses defines a trend with negative correlation from 500 to 380 Ma and Th/U values from 0.01 to 0.13. This correlation between the age and the composition of zircon suggests that the age dispersion is related to an actual geological process and is not caused by lead loss. Furthermore, even though the Th/U ratio shows a consistent evolution from 510 to 380 Ma, the rest of the proxies considered (Hf, Yb/Gd and Eu/Eu*, Figs. 13 a, b, c) point to a two-stage evolution, and the characteristics of the REE patterns are compatible with a metamorphic origin (Chen et al., 2009, 2010; Rubatto et al., 2009; Peters et al., 2013; Stipska et al., 2016).

This scenario is congruent with the presence of two metamorphic events in the HP-HT units, one at ~490-480 Ma and other at ~390-380 Ma (e.g., Fernández-Suárez et al., 2002, 2007). The increase in Yb/Gd values (Fig. 13 b), related to the slope of the HREE, in zircons aged from 502 to 430 Ma is congruent with a higher availability of HREE in the rock. As garnet is the most important HREE reservoir in metamorphic rocks, we argue that this behaviour is the record of the progressive destabilization of garnet in a decompressive path from HP-HT conditions. The increase observed in the Eu/Eu* ratio is consistent with a progressive destabilisation of plagioclase, which is the main europium reservoir in rocks (Barth and Wooden, 2010; Castiñeiras et al., 2011).

The sharp decrease observed in the Yb/Gd ratio from 420 to 380 Ma, is probably related to a new event of garnet growth (Rubatto et al., 2006; Stipska et al., 2016), i.e., the second HP-HT event. The evolution in the Eu/Eu* ratio suggests that this event took place under granulite facies conditions, as plagioclase was present to pump out all the available europium.

5.3. Monazite and titanite geochronology: Age of the youngest metamorphism in the Sobrado antiform

The youngest zircon data recorded (380 ± 4 Ma) is coherent with the monazite concordia age (382 ± 1 Ma) in the migmatitic paragneises of the Middle tectonic slice. Besides, both monazite and irregular/sub-round zircons share their microtextural setting along the migmatitic fabric, pointing to a coeval character with partial melting at relatively high-P. Furthermore, the chemical profiles observed in the monazite suggest simultaneous crystallization of this mineral with garnet (Rubatto, 2002; Rubatto et al., 2006; Mottram et al., 2014; Holder et al., 2015). Negative Eu anomalies indicate a preferential incorporation of europium to feldspars, in particular to K-feldspar, during melt crystallization (Buick et al., 2010; Rubatto et al., 2013). These characteristics are compatible with monazite crystallization in a single pulse (MSWD <1) in the presence of garnet, supporting its metamorphic origin. This Middle Devonian age can be interpreted to represent the *minimum* age of the youngest metamorphic event in Sobrado unit, which reached high-P granulite facies (Fernández-Suárez et al., 2007; Ordóñez Casado et al., 2001). It is suggested that monazite captures the onset of the exhumation process in the migmatitic paragneisses (Holder et al., 2015).

Titanite crystallization is synkinematic with the mylonitic fabric of the fine-grained amphibolites located at the base of the Upper tectonic slice. The growth of titanite in amphibolitic conditions is supportted by the umbrella-shaped REE patterns shown in Fig. 7b, typical of titanite coexisting with amphibole (Mulrooney and Rivers, 2005; Chambefort et al., 2013; Lesnov, 2013). A Late Devonian age (~365 Ma) could be related to the onset of retrograde metamorphic conditions during the development of the shear zone, and suggests a prolongated exhumation process, reaching amphibolite facies. The Late Devonian age lies close to the Ar-Ar exhumation ages of the uppermost units in the Órdenes complex as recorded in the Corredoiras detachment (376 ± 2.0 Ma in hornblende, Dallmeyer et al., 1997), or in the Ponte Carreira Detachment (371 ± 4.0 Ma in muscovite, Gómez Barreiro et al. 2006).

The U-Pb zircon age for the onset of the oldest metamorphic event was estimated using the TuffZirc method, developed by Ludwig and Mundil (2002), which calculates the median by choosing the largest set of concordant analyses that are statistically coherent. The best estimate obtained for this event is 489.58 (+ 12.15 - 6.76) Ma, obtained by pooling together only six of sixteen analyses (Fig. 16). The 510-380 Ma zircon aliquot shows a clear correlation between its cathodoluminescence texture and its geochemistry and could be also related to shielded population of "metamorphic" zircon grains within garnets (Fig. 4 e). The age recorded in the migmatitic paragneisses is thought to correspond to a metamorphic event, dated in the Early Ordovician (~490 Ma), and is in very good agreement with upper high-P/high-T dates of equivalent units carried out during previous studies (Kuijper, 1979; Peucat et al., 1990; Fernández-Suárez et al., 2002, 2007). This age also coincides with those obtained from intermediate-P units, where large plutons were emplaced and there is a lack of later high-P/high-T metamorphism during the Devonian. The westernmost upper intermediate-P units of the Órdenes Complex underwent a granulite-facies metamorphism dated between ca. 500 and 485 Ma, contemporaneous with the intrusion of massive gabbros and granodiorites related to Cambrian magmatic arc activity (Abati et al. al., 1999, 2003, 2007, 1999; Andonaegui et al., 2002, 2012, 2016; Castiñeiras et al., 2002, 2010). The granulite-facies metamorphism is associated with heating produced by the intrusions, accompanied by a quick burial, almost coeval with igneous emplacement (Abati et al., 2003; Castiñeiras, 2005; Fernández-Suárez et al., 2007).

Clearly, the metamorphic event recorded in some zircons is pre-Variscan and it is therefore independent of the high-P/high-T granulite-facies metamorphism that occurred during the Early-Middle Devonian that has been identified in the underlying upper units, such as in Sobrado with 660-770°C and 13-17 kbar (Arenas and Martínez Catalán, 2002), or 750-850°C and 12-15 kbar (Benítez-Pérez, 2017). The pre-Variscan metamorphism was probably followed by a decompression stage, associated with partial melting (Fernández-Suárez et al., 2002). Later on, HP-HT Devonian metamorphism occurred, during which exhumation through an isothermal decompression lead to partial melting in paragneisses and basic granulites (Fernández-Suárez et al., 2007). As the zircon composition and microstructural setting clearly suggests, the notable slope observed in the TuffZirc plot from 489 to 380 Ma (Fig. 16) is the result of these exhumation, burial and new exhumation processes accompanied by partial melting, in which the shielding role of garnet has played an important role.

6. Conclusions

This study provides new age constraints on the processes that have affected the Sobrado unit, part of the Órdenes Complex, and allows some correlation with events recognized in other parts of the allochthonous high-P/high-T complexes of NW Iberia. Titanite, monazite and zircon dating, together with REE analyses have been combined together in these rocks for the first time in order to carry out a geochronological investigation of the amphibolites and paragneisses.

According to the analyses, the youngest ages recorded by the metamorphic zircons are coherent with the concordia monazite age obtained from seventy-six analyses in the paragneisses. The microtextural setting of both metamorphic zircon and monazite along the HP-HT main foliation support that interpretation. Therefore, the Middle Devonian age (~380 Ma) represents the minimum age of the last Sobrado metamorphic event under high-P granulite-facies conditions and represents the first stages of the Variscan orogeny in this part of Iberia. Dating of metamorphic titanite in the amphibolite yields a Late Devonian age (~365 Ma) and is associated with very homogeneous REE patterns suggesting the prolongation of the exhumation process in the Sobrado unit, reaching amphibolite-facies metamorphic conditions. In zircon, there is a strong relationship between their textures, as seen in cathodoluminescence images (CL), REE patterns and $^{206}Pb/^{238}U$ ages. Metamorphic zircon defines an Early Ordovician age (~490 Ma) although showing a large dispersion. This date is linked to the first pre-Variscan granulite-facies metamorphism seen in in Sobrado unit under intermediate-P conditions, and it is interpreted to be related to the intrusion of basic and intermediate composition rocks, and coeval with burial in a magmatic arc context. Microstructural analysis of zircon, monazite and titanite provide complementary microtextural context to understand the origin of this population mixture. In situ dating should be conducted to confirm some textural relationships in the future.

The maximum depositional age of the Sobrado unit is suggested to be late Cambrian based on the age of the youngest inherited zircon (511 Ma). From the youngest set of inherited zircon, two ages can be obtained (546 and 526 Ma) , pointing to the formation of a peri-Gondwana magmatic arc. The protoliths of inherited zircon older than 1000 Ma from the Sobrado unit are found in other Iberian complexes and are thought to be related to sources mainly in the West African craton.

Data availability

The data are not publicly accessible

Supplement

There is no supplement related to this article.

Author contributions

JMBP, PC, JGB and JRMC contributed equally to the field, experimental and elaboration of the manuscript. AKC contributes to U-Pb-REE acquisition and data reduction and RH participated in the writing of the text and the geological interpretation.

Competing interests

The authors declare that they have no conflict of interest.

Acknowledgements

This paper has been funded by the research projects CGL2011-22728 and CGL2016-78560-P of the Spanish Ministry of Economy, Industry and Competitiveness, as part of the National Program of Projects in Fundamental Research. JMBP appreciate financial support by the Spanish Ministry of Economy, Industry and Competitiveness though the Formación de Profesional Investigador grant FPI 2013-2016 (BES-2012-059893). JGB appreciates financial support by the Spanish Ministry of Science and Innovation through the IEDI-2016-00691 fellowship. We kindly appreciate excelent reviews from M. Zucali, F. Rossetti, P. Ayarza and an anonymous referee which contributed to improve the manuscript.

References

Abati, J., Dunning, G.R., Arenas, R., Díaz García, F., González Cuadra, P., Martínez Catalán, J.R., Andonaegui, P., 1999. Early Ordovician orogenic event in Galicia (NW Spain): Evidence from U-Pb ages in the uppermost unit of the Ordenes Complex. Earth and Planetary Science Letters 165, 213–228. doi:10.1016/S0012-821X(98)00268-4

Abati, J., Arenas, R., Martinez Catalán, J.R., Díaz García, F., 2003. Anticlockwise P-T Path of Granulites from the Monte Castelo Gabbro (Ordenes Complex, NW Spain). Journal of Petrology 44, 305–327. doi:10.1093/petrology/44.2.305

Abati, J., Castiñeiras, P., Arenas, R., Fernández-Suárez, J., Barreiro, J.G., Wooden, J.L., 2007. Using SHRIMP zircon dating to unravel tectonothermal events in arc environments. The early Palaeozoic arc of NW Iberia revisited. Terra Nova 19, 432–439. doi:10.1111/j.1365-3121.2007.00768.x

Abati, J., Gerdes, A., Suárez, J.F., Arenas, R., Whitehouse, M.J., Fernández, R.D., 2010. Magmatism and early-Variscan continental subduction in the northern Gondwana margin recorded in zircons from the basal units of Galicia, NW Spain. Bulletin of the Geological Society of America 122, 219–235. doi:10.1130/B26572.1

Aerden, D.G.A.M., 2004. Correlating deformation in Variscan NW-Iberia using porphyroblasts; implications for the Ibero-Armorican Arc. Journal of Structural Geology 26, 177–196. doi:10.1016/S0191-8141(03)00070-1

Albert, R., Arenas, R., Gerdes, A., Sánchez-Martínez, S., Fernández-Suárez, J., Fuenlabrada, J.M., 2015. Provenance of the Variscan Upper Allochthon (Cabo Ortegal Complex, NW Iberian Massif). Gondwana Research 28, 1434–1448. doi:10.1016/j.gr.2014.10.016

Aleinikoff, J.N., Schenck, W.S., Plank, M.O., Srogi, L.A., Fanning, C.M., Kamo, S.L., Bosbyshell, H., 2006. Deciphering igneous and metamorphic events in high-grade rocks of the Wilmington complex, Delaware: Morphology, cathodoluminescence and backscattered electron zoning, and SHRIMP U-Pb geochronology of zircon and monazite. Bulletin of the Geological Society of America 118, 39–64. doi:10.1130/B25659.1

Aleinikoff, J.N., Wintsch, R.P., Tollo, R.P., Unruh, D.M., Fanning, C.M., Schmitz, M.D., 2007. Ages and origins of rocks of the Killingworth dome, south-central Connecticut: Implications for the tectonic evolution of southern New England. American Journal of Science 307, 63–118. doi:10.2475/01.2007.04

Álvarez-Valero, A.M., Gómez-Barreiro, J., Alampi, A., Castineiras, P., Martinez Catalán, J.R., 2014. Local isobaric heating above an extensional detachment in the middle crust of a Variscan allochthonous terrane (Ordenes complex, NW Spain). Lithosphere 6, 409–418. doi:10.1130/L369.1

Andonaegui, P., Castiñeiras, P., González Cuadra, P., Arenas, R., Sánchez Martínez, S., Abati, J., Díaz García, F., Martínez Catalán, J.R.., 2012. The Corredoiras orthogneiss (NW Iberian Massif): Geochemistry and geochronology of the Paleozoic magmatic suite developed in a peri-Gondwanan arc. Lithos 128–131, 84–99. doi:10.1016/j.lithos.2011.11.005

Andonaegui, P., González Del Tánago, J., Arenas, R., Abati, J., Martínez Catalán, J.R., Peinado, M., Díaz García, F., 2002. Tectonic setting of the Monte Castelo gabbro (Ordenes Complex, northwestern Iberian Massif): Evidence for an arc-related terrane in the hanging wall to the Variscan suture. Special Paper of the Geological Society of America 364, 37–56. doi:10.1130/0-8137-2364-7.37

Andonaegui, P., Sánchez-Martínez, S., Castiñeiras, P., Abati, J., Arenas, R., 2016. Reconstructing subduction polarity through the geochemistry of mafic rocks in a Cambrian magmatic arc along the Gondwana margin (Órdenes Complex, NW Iberian Massif). International Journal of Earth Sciences 105, 713–725. doi:10.1007/s00531-015-1195-x

Arenas, R., Martínez Catalán, J.R., 2002. Prograde development of corona textures in metagabbros of the Sobrado unit (Ordenes Complex, northwestern Iberian Massif). Geological Society of America Special Pa, 73–88. doi:10.1130/0-8137-2364-7.73

Bacon, C.R., Vazquez, J.A., Wooden, J.L., 2012. Peninsular terrane basement ages recorded by Paleozoic and Paleoproterozoic zircon in gabbro xenoliths and andesite from Redoubt volcano, Alaska. Bulletin of the Geological Society of America 124, 24–34. doi:10.1130/B30439.1

Ballèvre, M., Martínez Catalán J.R., López-Carmona, A., Pitra, P., Abati, J., Díez Fernández, R., Ducassou, C., Arenas, R., Bosse, V., Castiñeiras, P., Fernández-Suárez, J., Gómez Barreiro, J., Paquette, J-L., Peucat, J-J, Poujol, M., Ruffet, G. and Sánchez Martínez, S., 2014. Correlation of the nappe stack in the Ibero-Armorican arc across the Bay of Biscay: a joint French–Spanish project. Geological Society, London, Special Publications, 405, .doi: 10.1144/SP405.13

Barth, A.P., Wooden, J.L., 2010. Coupled elemental and isotopic analyses of polygenetic zircons from granitic rocks by ion microprobe, with implications for melt evolution and the sources of granitic magmas. Chemical Geology 277, 149–159. doi:10.1016/j.chemgeo.2010.07.017

Belousova, E.A., Griffin, W.L., O'Reilly, S.Y., Fisher, N.I., 2002. Igneous zircon: trace element composition as an indicator of source rock type. Contributions to Mineralogy and Petrology 143, 602–622. doi:10.1007/s00410-002-0364-7

Benítez-Pérez, J.M., 2017. Quantitative study of texture in tectonites by diffraction. Contribution to seismic anisotropy and orogenic rheology. University of Salamanca (PhD. Thesis). Spain.

Buick, I.S., Clark, C., Rubatto, D., Hermann, J., Pandit, M., Hand, M., 2010. Constraints on the Proterozoic evolution of the Aravalli-Delhi Orogenic belt (NW India) from monazite geochronology and mineral trace element geochemistry. Lithos 120, 511–528. doi:10.1016/j.lithos.2010.09.011

Castiñeiras, P., Andonaegui, P., Arenas, R., Martinez Catalán, J.., 2002. Descripción y resultados preliminares del plutón compuesto de San Xiao, Complejo de Cabo Ortegal (noroeste del Macizo Ibérico). Geogaceta 32, 111–114.

Castiñeiras, P., 2005. Origen y evolución tectonotermal de las unidades de O Pino y Cariño (Complejos Alóctonos de Galicia). Laboratorio Xeolóxico de Laxe, Serie Nova Terra, 28, A Coruña.

Castiñeiras, P., García, F.D., Gómez-Barreiro, J., 2010. REE-assisted U-Pb zircon age (SHRIMP) of an anatectic granodiorite: Constraints on the evolution of the A Silva granodiorite, Iberian allochthonous complexes. Lithos 116, 153–166. doi:10.1016/j.lithos.2010.01.013

Castiñeiras, P., Navidad, M., Casas, J.M., Liesa, M., Carreras, J., 2011. Petrogenesis of Ordovician Magmatism in the Pyrenees (Albera and Canigó Massifs) Determined on the Basis of Zircon Minor and Trace Element Composition. The Journal of Geology 119, 521–534. doi:10.1086/660889

Chen, R.X., Zheng, Y.F., Xie, L., 2010. Metamorphic growth and recrystallization of zircon: Distinction by simultaneous in-situ analyses of trace elements, U-Th-Pb and Lu-Hf isotopes in zircons from eclogite-facies rocks in the Sulu orogen. Lithos 114, 132–154. doi:10.1016/j.lithos.2009.08.006

Cheng, H., King, R.L., Nakamura, E., Vervoort, J.D., Zheng, Y.F., Ota, T., Wu, Y.B., Kobayashi, K., Zhou, Z.Y., 2009. Transitional time of oceanic to continental subduction in the Dabie orogen: Constraints from U-Pb, Lu-Hf, Sm-Nd and Ar-Ar multichronometric dating. Lithos 110, 327–342. doi:10.1016/j.lithos.2009.01.013

Cherniak, D.J., 2006. Zr diffusion in titanite. Contributions to Mineralogy and Petrology 152, 639–647. doi:10.1007/s00410-006-0133-0

Corfu, F., Hanchar, J.M., Hoskin, P.W.O., Kinny, P.D., 2003. Atlas of Zircon Textures, in: Hanchar, J.M., Hoskin, P.W.O. (Eds.), Zircon. Reviews in Mineralogy and Geochemistry. Mineralogical Society of America, pp. 468–500.

Corrie, S.L., Kohn, M.J., 2008. Trace-element distributions in silicates during prograde metamorphic reactions : implications for monazite formation 451–464. doi:10.1111/j.1525-1314.2008.00769.x

Dallmeyer, R.D., Martínez Catalán, J.R., Arenas, R., Gil Ibarguchi, J.I., Gutiérrez-Alonso, G., Farias, P., Bastida, F., Aller, J., 1997. Diachronous Variscan tectonothermal activity in the NW Iberian Massif: Evidence from 40Ar/39Ar dating of regional fabrics. Tectonophysics 277, 307–337. doi:10.1016/S0040-1951(97)00035-8

Dallmeyer, R.D., Ribeiro, A., Marques, F., 1991. Polyphase Variscan emplacement of exotic terranes (Morais and Bragança Massifs) onto Iberian successions: Evidence from 40Ar/39Ar mineral ages. Lithos 27, 133–144. doi:10.1016/0024-4937(91)90025-G

DeWolf, C.P., Belshaw, N., O'Nions, R.K., 1993. A metamorphic history from micron-scale 207pb/206pb chronometry of Archean monazite. Earth and Planetary Science Letters 120, 207–220.

Dias da Silva, I., Valverde-Vaquero, P., González-Clavijo, E., Díez-Montes, A. y Martínez Catalán, J. R. 2014. Structural and stratigraphical significance of U–Pb ages from the Mora and Saldanha volcanic complexes (NE Portugal, Iberian Variscides). In: Schulmann, K., Martínez Catalán, J. R., Lardeaux, J. M., Janousek, V. & Oggiano, G. (eds) The Variscan Orogeny: Extent, Timescale, the Formation of the European Crust. Geological Society, London, Special Publications, 405. First published online February 25, 2014, http://dx.doi.org/10.1144/SP405.3

Díaz García, F., Martínez Catalán, J.R., Arenas, R., González Cuadra, P., 1999. Structural and kinematic analysis of the Corredoiras detachment: evidence for early Variscan synconvergent extension in the Ordenes Complex, NW Spain. International Journal of Earth Sciences 88, 337–351.

Dickinson, W.R., Gehrels, G.E., 2009. Use of U-Pb ages of detrital zircons to infer maximum depositional ages of strata: A test against a Colorado Plateau Mesozoic database. Earth and Planetary Science Letters 288, 115–125. doi:10.1016/j.epsl.2009.09.013

Díez Fernández, R., Catalán, J.R.M., Gerdes, A., Abati, J., Arenas, R., Fernández-Suárez, J., 2010. U-Pb ages of detrital zircons from the Basal allochthonous units of NW Iberia: Provenance and paleoposition on the northern margin of Gondwana during the Neoproterozoic and Paleozoic. Gondwana Research 18, 385–399. doi:10.1016/j.gr.2009.12.006

Díez Fernández, R., Martínez Catalán, J.R., Arenas, R., Abati, J., Gerdes, A., Fernández-Suárez, J., 2012. U–Pb detrital zircon analysis of the lower allochthon of NW Iberia: age constraints, provenance and links with the Variscan mobile belt and Gondwanan cratons. Journal of the Geological Society 169, 655–665. doi:10.1144/jgs2011-146

Egal, E., Thiéblemont, D., Lahondère, D., Guerrot, C., Costea, C.A., Iliescu, D., Delor, C., Goujou, J.C., Lafon, J.M., Tegyey, M., Diaby, S., Kolié, P., 2002. Late Eburnean granitization and tectonics along the western and northwestern margin of the Archean K??n??ma-Man domain (Guinea, West African Craton). Precambrian Research 117, 57–84. doi:10.1016/S0301-9268(02)00060-8

Ennih, N., Liegeois, J.-P., 2008. The boundaries of the West African craton, with special reference to the basement of the Moroccan metacratonic Anti-Atlas belt. The Boundaries of the West African Craton 1–17. doi:10.1144/SP297.1

Farias, P., Gallastegui, G. et al. 1987. Aportaciones al conocimiento de la litoestratigrafía y estructura de Galicia Central. Memo´rias da Faculdade de Ciências, Universidade do Porto, 1, 411–431.

Fernández-Suárez, J., Arenas, R., Abiati, J., Martinez Catalán, J.R., Whitehouse, M., Jeffries, T., 2007. U-Pb chronometry of polymetamorphic high-pressure granulites: An example from the allochthonous terranes of the NW Iberian Variscan belt. Geological Society of America Memoir, 469–488. doi:10.1130/2007.1200(24).

Fernández-Suárez, J., Corfu, F., Arenas, R., Marcos, A., Martínez Catalán, J.R., Díaz García, F., Abati, J., Fernández, F.J., 2002. U-Pb evidence for a polyorogenic evolution of the HP-HT units of the NW Iberian Massif. Contributions to Mineralogy and Petrology 143, 236–253. doi:10.1007/s00410-001-0337-2

Fernández-Suárez, J., Garcia, F.D., Jeffries, T.E., Arenas, R., 2003. Constraints on the provenance of the uppermost allochthonous terrane of the NW Iberian Massif: inferences from detrital zircon U-Pb ages. Terra Nova 15, 138–144.

Franz, G., Spear, F.S., 1985. Aluminous Titanite (sphene) fremo the eclogite zone, south-central Tauern window, Austria. Chemical Geology 50, 33–46.

Frost, B.R., Chamberlain, K.R., Schumacher, J.C., 2000. Sphene (titanite): phase relations and role as a geochronometer. Chemical Geology 172, 131–148.

Fuenlabrada, J., Arenas, R., Sánchez-Martínez, S., Díaz García, F., Castiñeiras, P., 2010. A peri-Gondwanan arc in NW Iberia I: Isotopic and geochemical constraints on the origin of the arc-A sedimentary approach. Gondwana Research 17, 338–351. doi:10.1016/j.gr.2009.09.007

Gagnevin, D., Daly, J.S., 2010. Zircon texture and chemical composition as a guide to magmatic processes and mixing in a granitic environment and coeval volcanic system. doi:10.1007/s00410-009-0443-0

Gómez Barreiro, J., Wijbrans, J.R., Castiñeiras, P., Martínez Catalán, J.R., Arenas, R., Díaz García, F. and Abati, J., 2006. $^{40}Ar/^{39}Ar$ laserprobe dating of mylonitic fabrics in a polyorogenic terrane of NW Iberia. Journal of the Geological Society, 163(1), pp.61-73. https://doi.org/10.1144/0016-764905-012.

Gómez-Barreiro, J., Martínez Catalán, J.R., Arenas, R., Castiñeiras, P., Abati, J., Díaz García, F., Wijbrans, J.R., 2007. Tectonic evolution of the upper allochthon of the Órdenes complex (northwestern Iberian Massif): Structural constraints to a polyorogenic peri-Gondwanan terrane. Geological Society of America 423, 315–332. doi:10.1130/2007.2423(15).

Goncalves, P., Williams, M.L., Jercinovic, M.J., 2005. Electron-microprobe age mapping of monazite. American Mineralogist 90, 578–585. doi:10.2138/am.2005.1399

Grimes, C.B., Wooden, J.L., Cheadle, M.J., John, B.E., 2015. "Fingerprinting" tectono-magmatic provenance using trace elements in igneous zircon. Contributions to Mineralogy and Petrology 170, 1–26. doi:10.1007/s00410-015-1199-3

Gutiérrez-Alonso, G., Fernández-Suárez, J., Jeffries, T.E., Jenner, G.A., Tubrett, M.N., Cox, R., Jackson, S.E., 2003. Terrane accretion and dispersal in the northern Gondwana margin. An Early Paleozoic analogue of a long-lived active margin. Tectonophysics 365, 221–232. doi:10.1016/S0040-1951(03)00023-4

Hacker, B.R., Kylander-clark, A.R.C., Holder, R., Andersen, T.B., Peterman, E.M., Walsh, E.O., Munnikhuis, J.K., 2015. Monazite response to ultrahigh-pressure subduction from U – Pb dating by laser ablation split stream. Chemical Geology 409, 28–41. doi:10.1016/j.chemgeo.2015.05.008

Hanchar, J.M., Westrenen, W. Van, 2007. Rare earth element behavior in zircon–melt systems. Elements 3, 37–42.

Harlov, D., Tropper, P., Seifert, W., Nijland, T., Förster, H.-J., 2006. Formation of Al-rich titanite (CaTiSiO4 O – CaAlSiO 4 OH) reaction rims on ilmenite in metamorphic rocks as a function of f H2O and f O2. Lithos 88, 72–84. doi:10.1016/j.lithos.2005.08.005

Hawkins, D.P., Bowring, S.A., 1997. U-Pb systematics of monazite and xenotime : case studies from the Paleoproterozoic of the Grand Canyon, Arizona 87–103.

Hermann, J., Rubatto, D., 2003. Relating zircon and monazite domains to garnet growth zones : Age and duration of granulite facies metamorphism in the Val Malenco lower crust. Journal of Metamorphic 21, Issue 9. doi:10.1046/j.1525-1314.2003.00484.x

Hokada, T., Harley, S.L., 2004. Zircon growth in UHT leucosome: constraints from zircon-garnet rare earth elements (REE) relations in Napier Complex, East Antarctica. Journal of Mineralogical and Petrological Sciences 99, 180–190. doi:10.2465/jmps.99.180

Holder, R.M., Hacker, B.R., Kylander-clark, A.R.C., Cottle, J.M., 2015. Monazite trace-element and isotopic signatures of (ultra) high-pressure metamorphism : Examples from the Western Gneiss Region, Norway. Chemical Geology 409, 99–111. doi:10.1016/j.chemgeo.2015.04.021

Horstwood, M.S.A., Foster, G.L., Parrish, R.R., Noble, S.R., Nowell, G.M., 2003. Common-Pb corrected in situ U–Pb accessory mineral geochronology by LA-MC-ICP-MS. The Royal Society of Chemistry 18, 837–846. doi:10.1039/b304365g

Hoskin, P.W.O., 2005. Trace-element composition of hydrothermal zircon and the alteration of Hadean zircon from the Jack Hills, Australia. Geochimica et Cosmochimica Acta 69, 637–648. doi:10.1016/j.gca.2004.07.006

Hoskin, P.W.O., Ireland, T.R., 2000. Rare earth element chemistry of zircon and its use as a provenance indicator. Geology 28, 627–630. doi:10.1130/0091-7613(2000)28<627:REECOZ>2.0.CO

Hoskin, P.W.O., Schaltegger, U., 2003. The Composition of Zircon and Igneous and Metamorphic Petrogenesis, in: Hanchar, J.M., Hoskin, P.W.O. (Eds.), Zircon. Reviews in Mineralogy and Geochemistry. Mineralogical Society of America, pp. 27–62.

Jackson, S.E., Pearson, N.J., Griffin, W.L., Belousova, E.A., 2004. The application of laser ablation-inductively coupled plasma-mass spectrometry to in situ U-Pb zircon geochronology. Chemical Geology 211, 47–69. doi:10.1016/j.chemgeo.2004.06.017

Ji, S., Martignole, J., 1994. Ductility of garnet as an indicator of extremely high temperature deformation.

Journal of Structural Geology 16, 985‐996.

Kleinschrodt, R., Duyster, J., 2002. HT-deformation of garnet: an EBSD study on granulites from Sri Lanka, India and the Ivrea Zone. Journal of Structural Geology 24, 1829‐1844.

Kohn, M.J., Malloy, M.A., 2004. Formation of monazite via prograde metamorphic reactions among common silicates : Implications for age determinations. Geochimica et cosmochimica Acta 68, 101–113. doi:10.1016/S0016-7037(03)00258-8

Košler, J., Tubrett, M.N., Sylvester, P.J., 2001. Application of laser ablation ICP-MS to U-Th-Pb dating of monazite. Geostandards Newsletter-the Journal of Geostandards and Geoanalysis 25, 375–386. doi:10.1111/j.1751-908X.2001.tb00612.x

Kretz, R., 1983. Symbols for rock-forming minerals. American Mineralogist 68, 277–279. doi:10.1016/0016-7037(83)90220-X

Kuijper, R.P., 1979. U-Pb systematic and petrogenetic evolution of infracrustal rocks in the Paleozoic basement of Western Galicia, NW Iberia. WO Laboratory of Isotope Geology, Amsterdam.

Kylander-Clark, A.R.C., Hacker, B.R., Cottle, J.M., 2013. Laser-ablation split-stream ICP petrochronology. Chemical Geology 345, 99–112. doi:10.1016/j.chemgeo.2013.02.019

Lesnov, F.P., 2013. Consistent patterns of rare earth element distribution in accessory minerals from rocks of mafic-ultramafic complexes. Central European Journal of Geosciences 5, 112–173. doi:10.2478/s13533-012-0121-z

Linnemann, U., Gerdes, A., Hofmann, M., Marko, L., 2014. The Cadomian Orogen: Neoproterozoic to Early Cambrian crustal growth and orogenic zoning along the periphery of the West African Craton-Constraints from U-Pb zircon ages and Hf isotopes (Schwarzburg Antiform, Germany). Precambrian Research 244, 236–278. doi:10.1016/j.precamres.2013.08.007

Ludwig, K.R., 1998. On the Treatment of Concordant Uranium-Lead Ages. Geochimica et Cosmochimica Acta 62, 665–676. doi:10.1016/S0016-7037(98)00059-3

Ludwig, K.R., Mundil, R., 2002. Extracting reliable U–Pb ages and errors from complex populations of zircons from Phanerozoic tuffs. Geochimica et Cosmochimica Acta 66, 463.

Ludwig, K.R., 2012. User's Manual for ISOPLOT version 3.75. A Geochronological Toolkit for Microsoft Excel. Berkeley Geochronology Center.

Martínez Catalán, J.R., Arenas, R., Díaz García, F., Abati, J., 1999. Allochthonous Units in the Variscan Belt of NW Iberia: Terranes and Accretionary History, in: Sinha, A.K. (Ed.), Basement Tectonics 13: Proceedings of the Thirteenth International Conference on Basement Tectonics Held in Blacksburg, Virginia, U.S.A., June 1997. Springer Netherlands, Dordrecht, pp. 65–84. doi:10.1007/978-94-011- 4800-9_5

Martínez Catalán, J.R., Fernández-Suárez, J., Jenner, G.A., Belousova, E., Díez Montes, A., 2004, Provenance constraints from detrital zircon U–Pb ages in the NW Iberian Massif: implications for Paleozoic plate configuration and Variscan evolution. J. Geol. Soc. London, 161, 461–473. doi:10.1144/0016-764903-054

Martínez Catalán, J.R., Arenas, R., Abati, J., Sánchez Martínez, S., Díaz García, F., Fernández Suárez, J., González Cuadra, P., Castiñeiras, P., Gómez Barreiro, J., Díez Montes, A., González Clavijo, E., Rubio Pascual, F.J., Andonaegui, P., Jeffries, T.E., Alcock, J.E., Díez Fernández, R., López Carmona, A., 2009. A rootless suture and the loss of the roots of a mountain chain: The Variscan belt of NW Iberia. Comptes Rendus Geoscience 341, 114–126. doi:10.1016/j.crte.2008.11.004

Martínez Catalán, J.R., 2011. Are the oroclines of the Variscan belt related to late Variscan strike-slip tectonics? Terra Nova 23, 241–247. doi:10.1111/j.1365-3121.2011.01005.x

Martínez Catalán, J.R., 2012. The Central Iberian arc, an orocline centered in the Iberian Massif and some implications for the Variscan belt. International Journal of Earth Sciences 101, 1299–1314. doi:10.1007/s00531-011-0715-6

McDonough, W.F., Sun, S.S., 1995. The composition of the Earth. Chemical Geology 120, 223–253. doi:10.1016/0009-2541(94)00140-4

Möller, A., O'Brien, P.J., Kennedy, A., Kröner, A., 2002. Polyphase zircon in ultrahigh-temperature granulites (Rogaland, SW Norway): Constraints for Pb diffusion in zircon. Journal of Metamorphic Geology 20, 727–740. doi:10.1046/j.1525-1314.2002.00400.x

Mottram, C.M., Warren, C.J., Regis, D., Roberts, N.M.W., Harris, N.B.W., Argles, T.W., Parrish, R.R., 2014. Developing an inverted barrovian sequence; insights from monazite petrochronology. Earth and Planetary Science Letters 403, 418–431. doi:10.1016/j.epsl.2014.07.006

Mulrooney, D., Rivers, T., 2005. Redistribution of the rare-earth elements among coexisting minerals in metamafic rocks across the epidote-out isograd: An example from the St. Anthony Complex, northern Newfoundland, Canada. Canadian Mineralogist 43, 263–294. doi:10.2113/gscanmin.43.1.263

Nasdala, L., Zhang, M., Kempe, U., Panczer, G., Gaft, M., Andrut, M., Plötze, M., 2003. Spectroscopic methods applied to zircon, in: Hanchar, J.M., Hoskin, P.W.O. (Eds.), Zircon. Reviews in Mineralogy and Geochemistry. Mineralogical Society of America, pp. 427–467.

Ordóñez Casado, B., 1998. Geochronological studies of the pre-Mesozoic basement of the Iberian Massif : the Ossa Morena zone and the Allochthonous Complexes within the Central Iberian zone. PhD Thesis, Swiss Federal Institute of Technology, Zürich, Switzerland, 235 pp., doi:10.3929/ethz-a-002017279

Ordóñez Casado, B., Gebauer, D., Schäfer, H.J., Ibarguchi, J.I.G., Peucat, J.J., 2001. A single Devonian subduction event for the HP/HT metamorphism of the Cabo Ortegal complex within the Iberian Massif. Tectonophysics 332, 359–385. doi:10.1016/S0040-1951(00)00210-9

Pablo Maciá, J.G. de, and Martínez Catalán, J.R. 1984. Estructura, petrología y evolución de la región de Sobrado de los Monjes (La Coruña). Cuadernos do Laboratorio Xeolóxico de Laxe 7, 103–124.

Palin, R.M., Searle, M.P., Waters, D.J., Parrish, R.R., Roberts, N.M.W., Horstwood, M.S.A., Yeh, M.W., Chung, S.L., Anh, T.T., 2013. A geochronological and petrological study of anatectic paragneiss and associated granite dykes from the Day Nui Con Voi metamorphic core complex, North Vietnam: Constraints on the timing of metamorphism within the Red River shear zone. Journal of Metamorphic Geology 31, 359–387. doi:10.1111/jmg.12025

Passchier, C. W., and Trouw, R. A. (2005). Microtectonics. Springer Science & Business Media.

Paton, C., Hellstrom, J., Paul, B., Woodhead, J., Hergt, J., 2011. Iolite: Freeware for the visualisation and processing of mass spectrometric data. Journal of Analytical Atomic Spectrometry 26, 2508. doi:10.1039/c1ja10172b

Peters, T.J., Ayers, J.C., Gao, S., Liu, X.M., 2013. The origin and response of zircon in eclogite to metamorphism during the multi-stage evolution of the Huwan Shear Zone, China: Insights from Lu-Hf and U-Pb isotopic and trace element geochemistry. Gondwana Research 23, 726–747. doi:10.1016/j.gr.2012.05.008

Peucat, J.J., Bernard Griffiths, J., Ibarguchi, J.I.G., Dallmeyer, R.D., Menot, R.P., Cornichet, J., Ponce de León, M.I., 1990. Geochemical and Geochronological Cross-Section of the Deep Variscan Crust - the Cabo-Ortegal High-Pressure Nappe (Northwestern Spain). Tectonophysics 177, 263–292.

Peucat, J.J., Capdevila, R., Drareni, A., Mahdjoub, Y., Kahoui, M., 2005. The Eglab massif in the West African Craton (Algeria), an original segment of the Eburnean orogenic belt: Petrology, geochemistry and geochronology. Precambrian Research 136, 309–352. doi:10.1016/j.precamres.2004.12.002

Potrel, A., Peucat, J.J., Fanning, C.M., 1998. Archean crustal evolution of the West African Craton: example of the Amsaga Area (Reguibat Rise). U-Pb and Sm-Nd evidence for crustal growth and recycling. Precambrian Research 90, 107–117. doi:10.1016/S0301-9268(98)00044-8

Ribeiro, A., Pereira, E. & Dias, R. 1990. Central-Iberian Zone. Allochthonous Sequences. Structure in the Northwest of the Iberian Peninsula. In: Dallmeyer, R. D. y Martínez García, E. (eds) Pre-Mesozoic Geology of Iberia. Springer, Berlin, 220–236.

Rubatto, D., Hermann, J., 2001. Exhumation as fast as subduction ? Geology 29, 3–6.

Rubatto, D., 2002. Zircon trace element geochemistry : distribution coefficients and the link between U-Pb ages and metamorphism Zircon trace element geochemistry : partitioning with garnet and the link between U – Pb ages and metamorphism. Chemical Geology 184, 123–138.

Rubatto, D., Hermann, R.G., Buick, I.S., 2006. Temperature and Bulk Composition Control on the Growth of Monazite and Zircon During Low-pressure Anatexis (Mount Stafford , Central Australia). Journal of Petrology 47, 1973–1996. doi:10.1093/petrology/egl033

Rubatto, D., Hermann, J., Berger, A., Engi, M., 2009. Protracted fluid-induced melting during Barrovian metamorphism in the Central Alps. Contributions to Mineralogy and Petrology 158, 703–722. doi:10.1007/s00410-009-0406-5

Rubatto, D., Chakraborty, S., Dasgupta, S., 2013. Timescales of crustal melting in the Higher Himalayan Crystallines (Sikkim, Eastern Himalaya) inferred from trace element-constrained monazite and zircon chronology. Contributions to Mineralogy and Petrology 165, 349–372. doi:10.1007/s00410-012-0812-y

Santos Zalduegui, J.F., Schärer, U., Gil Ibarguchi, J.I., 1995. Isotope constraints on the age and origin of magmatism and metamorphism in the Malpica-Tuy allochthon, Galicia, NW Spain. Chemical Geology 121, 91–103. doi:10.1016/0009-2541(94)00123-P

Santos Zalduegui, J.F., Schärer, U., Gil Ibarguchi, J.I., Girardeau, J., 1996. Origin and evolution of the Paleozoic Cabo Ortegal ultramafic-mafic complex (NW Spain): U-Pb, Rb-Sr and Pb-Pb isotope data. Chemical Geology 129, 281–304. doi:10.1016/0009-2541(95)00144-1

Santos Zalduegui, J.F., Scharer, U., Gil Ibarguchi, J.I., Girardeau, J., 2002. Genesis of Pyroxenite-rich Peridotite at Cabo Ortegal (NW Spain): Geochemical and Pb-Sr-Nd Isotope Data. J. Petrol. 43, 17–43. doi:10.1093/petrology/43.1.17

Schaltegger, U., Fanning, C.M., Günter, D., Maurin, J.C., Schulmann, K., Gebauer, D., 1999. Growth, annealing and recrystallization of zircon and preservation of monazite in high-grade metamorphism: conventional and in-situ U-Pb isotope, cathodoluminescence and microchemical evidence. Contributions to Mineralogy and Petrology 134, 186–201.

Schofield, D.I., Horstwood, M.S.A., Pitfield, P.E.J., Gillespie, M., Darbyshire, F., O'Connor, E.A., Abdouloye, T.B., 2012. U-Pb dating and Sm-Nd isotopic analysis of granitic rocks from the Tiris Complex: New constaints on key events in the evolution of the Reguibat Shield, Mauritania. Precambrian Research 204–205, 1–11. doi:10.1016/j.precamres.2011.12.008

Spear, F.S., 1981. An experimental study of hornblende stability and compositional variability in amphibolite. American Journal of Science. doi:10.2475/ajs.281.6.697

Spear, F.S., Pyle, J.M., 2002. Apatite , Monazite , and Xenotime in Metamorphic Rocks, in: Kohn, M.J., Rakovan, J., Hughes, J.M. (Eds.), Phosphates: Geochemical, Geobiological, and Materials Importance. Reviews in Mineralogy and Geochemistry. doi:10.2138/rmg.2002.48.7

Spencer, K.J., Hacker, B.R., Kylander-clark, A.R.C., Andersen, T.B., Cottle, J.M., Stearns, M.A., Poletti, J.E., Seward, G.G.E., 2013. Campaign-style titanite U – Pb dating by laser-ablation ICP : Implications for crustal fl ow , phase transformations and titanite closure. Chemical Geology 341, 84–101. doi:10.1016/j.chemgeo.2012.11.012

Stearns, M.A., Cottle, J.M., Hacker, B.R., Kylander-Clark, A.R.C., 2016. Extracting thermal histories from the near-rim zoning in titanite using coupled U-Pb and trace-element depth profiles by single-shot laser-ablation split stream (SS-LASS) ICP-MS. Chemical Geology 422, 13–24. doi:10.1016/j.chemgeo.2015.12.011

Stearns, M.A., Hacker, B.R., Ratschbacjer, L., Rutte, D., Kylander-clark, A.R.C., 2015. Titanite petrochronology of the Pamir gneiss domes: Implications for middle to deep crust exhumation and titanite closure to Pb and Zr diffusion. Tectonics 34, 784–802. doi:10.1002/2014TC003774.Received

Stipska, P., Powell, R., Hacker, B.R., Holder, R., 2016. Uncoupled U / Pb and REE response in zircon during the transformation of eclogite to mafic and intermediate granulite (Blansk y les , Bohemian Massif). Journal of Meta 34, 551–572. doi:10.1111/jmg.12193

Storey, C.D., Smith, M.P., Jeffries, T.E., 2007. In situ LA-ICP-MS U – Pb dating of metavolcanics of Norrbotten , Sweden : Records of extended geological histories in complex titanite grains. Chemical Geology 240, 163–181. doi:10.1016/j.chemgeo.2007.02.004

Stübner, K., Grujic, D., Parrish, R.R., Roberts, N.M.W., Kronz, A., Wooden, J., Ahmad, T., 2014. Lithos Monazite geochronology unravels the timing of crustal thickening in NW Himalaya. LITHOS 210–211, 111–128. doi:10.1016/j.lithos.2014.09.024

Tera, F., Wasserburg, G.J., 1972. U-Th-Pb systematics in three Apollo 14 basalts and the problem of initial Pb in lunar rocks. Earth and Planetary Science Letters 14, 281–304. doi:10.1016/0012-821X(72)90128-8

Terry, M.P., Hamilton, M.A., 2000. Monazite geochronology of UHP and HP metamorphism , deformation , and exhumation , Nordoyane ... doi:10.2138/am-2000-11-1208

Tomascak, P.B., Krogstad, E.J., Walker, R.J., 1996. U-Pb Monazite Geochronology of Granitic Rocks from Maine: Implications for Late Paleozoic Tectonics in the Northern Appalachians. The Journal of Geology 104, 185–195.

Verts, L.A., Frost, C.D., 1996. U-Pb sphene dating of metamorphism : the importance of sphene growth in the contact aureole of the Red Mountain pluton , Laramie Mountains , Wyoming. Contributions to Mineralogy and Petrology 125, 186–199.

Watson, E.B., Yan Liang, 1995. A simple model for sector zoning in slowly grown crystals: implications for growth rate and lattice diffusion, with emphasis on accessory minerals in crustal rocks. American Mineralogist 80, 1179–1187.

Whitehouse, M.J., Platt, Æ.J.P., 2003. Dating high-grade metamorphism - constraints from rare-earth elements in zircon and garnet. Contributions to Mineralogy and Petrology 145, 61–74. doi:10.1007/s00410-002-0432-z

Whitney, D. L., Evans, B. W. (2010). Abbreviations for names of rock-forming minerals. American mineralogist, 95(1), 185-187. https://doi.org/10.2138/am.2010.3371

Wieldenbeck, M., Allé, P., Corfú, F., Griffin, W.L., Meier, M., Oberli, F., Quadt, A. Von, Roddick, J.C., Spiegel, W., 1995. Three Natural Zircon Standards for U-Th-Pb, Lu-Hf, Trace Element and REE Analyses. Geostandards Newsletter 19, 1–23. doi:10.1111/j.1751-908X.1995.tb00147.x

Williams, M.L., Jercinovic, M.J., Hetherington, C.J., 2007. Microprobe Monazite Geochronology: Understanding Geologic Processes by Integrating Composition and Chronology. Annual Review of Earth and Planetary Sciences 35, 137–175. doi:10.1146/annurev.earth.35.031306.140228

Zeck, H.P., Wingate, M.T.D., Pooley, G.D., Ugidos, J.M., 2004. A Sequence of Pan-African and Hercynian Events Recorded in Zircons from an Orthogneiss from the Hercynian Belt of Western Central Iberia —an Ion Microprobe U– Pb Study 45, 1613–1629. doi:10.1093/petrology/egh026

Zeringue, J., Bowring, J.~F., McLean, N.~M., Pastor, F., 2014. Building Interactive Visualizations for Geochronological Data. AGU Fall Meeting Abstracts.

Zhu, X.K., O'Nions, R.K., Belshaw, N.S., Gibb, A.J., 1997. Significance of in situ SIMS chronometry of zoned monazite from the Lewisian granulites, northwest Scotland. Chemical Geology 5, 35–53.

FIGURE CAPTIONS

Figure 1. (a) Simplified map of the Variscan orogen in Europe with the location of the Órdenes Complex. (b) Map of the Órdenes Complex with indication of the main units and tectonic contacts. Extensional detachments are labeled: BPSD, Bembibre-Pico Sacro system; CD: Corredoiras; FD, Fornás; PCD, Ponte Carreira. Fig. 2 location indicated.

Figure 2. Geological map of the study area and location of the samples, modified from Arenas and Martínez Catalán (2002): (a) Location of the Órdenes complex within the Iberian massif. (b) Sobrado Unit map, indicating units and tectonic slices. (c) Cross-section in WNW-ESE direction and (d) SW-NE and SSW-NNE direction of the Sobrado antiform. Sample location are indicated.

Figure 3. Fine grained amphibolites (sample JBP-71-21) from the basal mylonitic band in the Sobrado Upper tectonic slice. (a) Hornblende-plagioclase mixtures and titanite with preferred orientation, defining the mylonitic fabric. (b) Main fabric surrounding a garnet porfiroclast. Note titanite is the Ti phase in the mylonitic fabric but ilmenite grains have been preserved inside the garnet. The position of (c) is indicated by a white dashed square. (c) Garnet inclusions from (b) where ilmenite inclusions show a progressive breakdown into titanite (Ilm>Ttn). Note ilmenite inclusions inside pristinte garnet areas show no evidence of transformation. (d) Inclusions of rutile inside titanite and partial transformation of plagioclase into zoisite. All micrographs in plane-polarized light (PPL). (Mineral abbreviations after Whitney and Evans, 2010; Hbl: hornblende, Ttn: titanite, Ilm: ilmenite, Rt: rutile, Pl: plagioclase, Zo: zoisite, Grt: garnet).

Figure 4. Granulite facies migmatitic paragneiss from the Sobrado Middle tectonic slice (Fig. 2). (a) General microstructure where leucosome bands and preferred orientation of elongated garnets, biotite, rutile and kyanite define the foliation. (b) Zircon elongated grain in recrystallized leucosome domain. Main inclusions in garnet include rutile, ilmenite and zircon (PPL) and (c) Cross-polarized ligth (CPL). (d) Monazite and zircon subrounded grain in the leucosome domain. (e) Subrounded elongated grain of zircon included in a garnet. (f) Plastically deformed garnet (sigmoidal grain) in a leucosome. Zircon and monazite are found in the quartz-rich area around the garnet. (g) Sigmoidal garnet in a leucosome. Inclusions of prismatic and bipiramidal zircons and rutile are observed. (h) Monazite grain in a garnet pressure shadow with biotite. Ky: kyanite, Bt: biotite, Qtz: quartz, Kfs: K-felspard, Pl: plagioclase, Rt: rutile, Zrn: zircon, Mnz: monazite, Grt: garnet.

Figure 5. (a) Monazite grain compositional maps in paragneiss with a 30% thorium variation. Location and spot numbers (46 and 47) are indicated, as well as the $^{206}Pb/^{238}U$ age and error ($\pm 2\sigma$). (b) Chondrite-normalized rare earth element (REE) patterns for the same monazites in (a).

Figure 6. Cathodoluminescence (CL) images with the location of the analyzed spots for selected zircon grains.

Figure 7. (a) Tera-Wasserburg diagram showing distribution of analysed titanites (n = 51) from Sobrado amphibolite (JBP-71-21). The rejected analyses are represented by gray ellipses. The ellipses represent the $^{207}Pb/^{206}Pb$ and $^{238}U/^{206}Pb$ errors ($\pm 2\sigma$). (b) Chondrite-normalized rare earth element (REE) patterns for the same titanites.

Figure 8. (a) Tera-Wasserburg diagram showing distribution of analysed monazites (n = 76) from Sobrado paragneiss (JBP-71-15). The rejected analyses are represented by gray ellipses. The ellipses represent the $^{207}Pb/^{206}Pb$ and $^{238}U/^{206}Pb$ errors ($\pm 2\sigma$). (b) Chondrite-normalized rare earth element (REE) patterns for the same monazites.

Figure 9. Concordia plot (a) including all zircon with concordance >90% from sample JBP-71-15 (Sobrado migmatitic paragneiss), and (b) age histogram and probability density plot for ages older than 1000 Ma.

Figure 10. Tera-Wasserburg diagram (a) for the analyses between 589 and 380 Ma, and, (b) age histogram and probability density plot for the same ages.

Figure 11. Chondrite-normalized plots for inherited zircon older than 1000 Ma.

Figure 12. Chondrite-normalized plots for zircon between 589 and 380 Ma.

Figure 13. (a) Hafnium versus age, (b) Yb/Gd versus age, (c) Eu/Eu* versus age, and (d) U/Ce versus Th for zircon analyses between 589 and 380 Ma.

Figure 14. Th/U ratio versus $^{206}Pb/^{238}U$ ages for the zircon analyses from 589 to 380 Ma. Analysis 63 (510 Ma) is not represented as it has an anomalous value (6.59).

Figure 15. Weigthed average obtained from magmatic ages distributed between 589 and 510 Ma.

Figure 16. Age of the onset of the oldest HP-HT metamorphic event obtained using the TuffZirc algorythm.

Table 1: U-Th_Pb+REE Titanite_McD_S

Table 2A: U-Th_Pb+REE Monazite_McD_S

Table 3: U-Th_Pb Zircon sorted by age

Table 4A: REE Zircon_McD_S sorted by age

Table 4B: REE Zircon_McD_S sorted by age

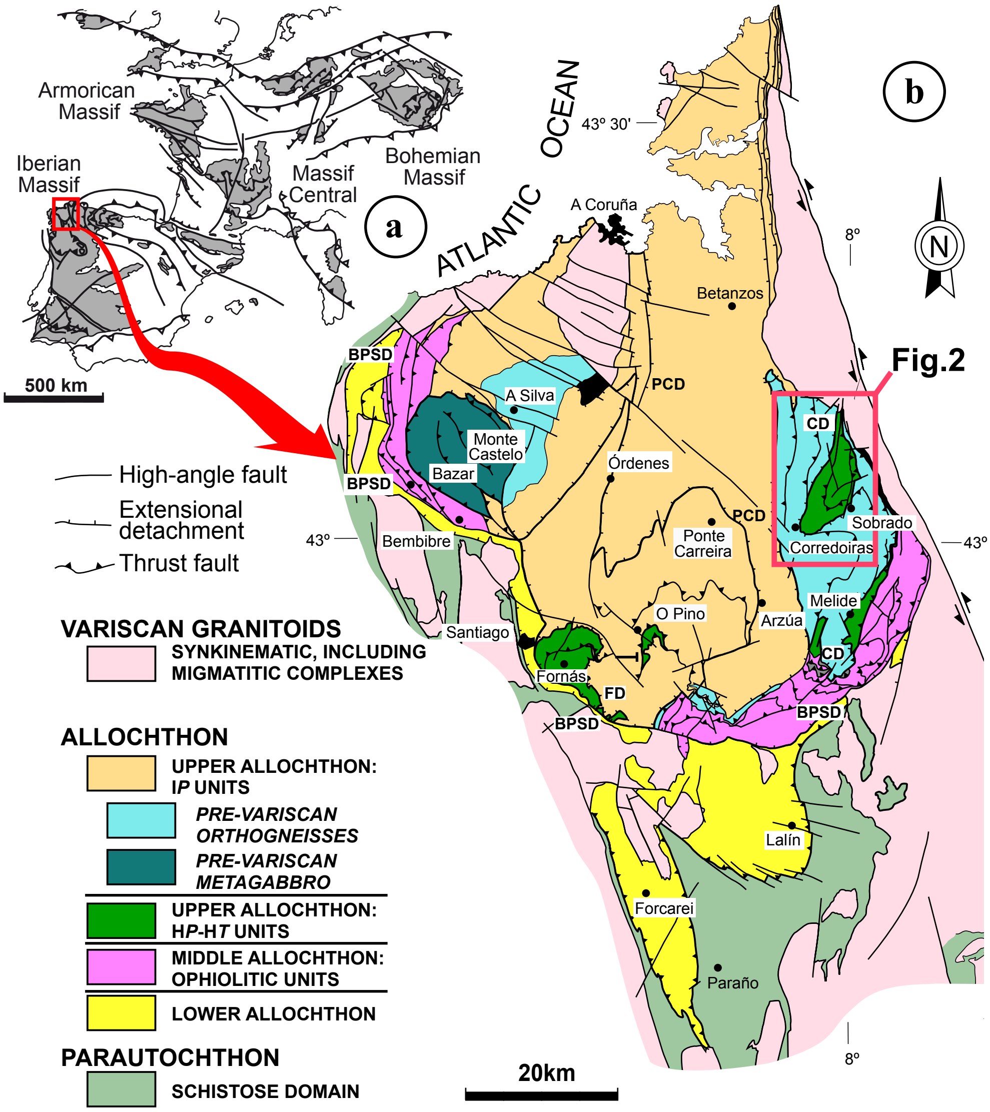

Figure 1: a) Simplified map of the Variscan orogen in Europe with the location of the Órdenes Complex. b) Map of the Órdenes Complex with indication of the main units and tectonic contacts. Extensional detachments are labeled: BPSD, Bembibre-Pico Sacro system; CD: Corredoiras; FD, Fornás; PCD, Ponte Carreira. Fig. 2 location indicated.

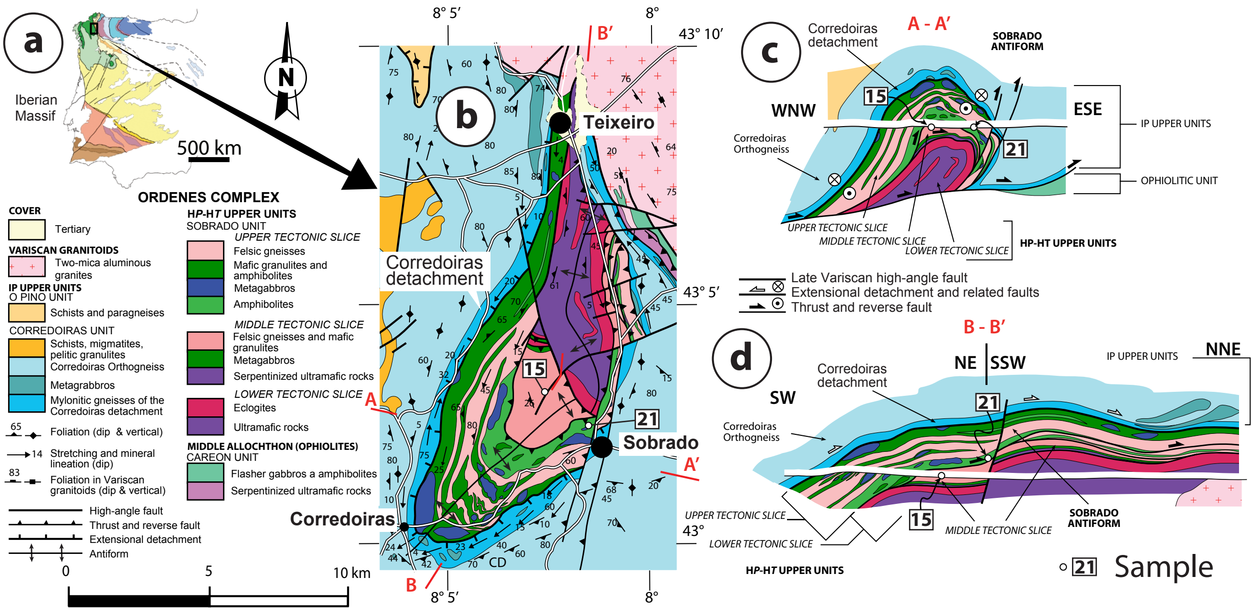

Figure 2. Geological map of the study area and location of the samples, modified from Arenas and Martínez Catalán (2002): (a) Location of the Órdenes complex within the Iberian massif. (b) Sobrado Unit map, indicating units and tectonic slices. (c) Cross-section in WNW-ESE direction and (d) SW-NE and SSW-NNE direction of the Sobrado antiform. Sample location are indicated.

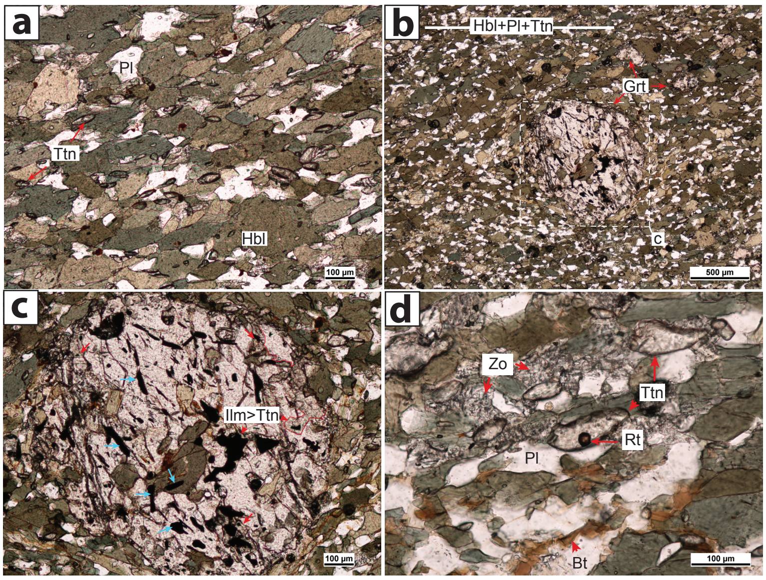

Figure 3. Fine grained amphibolites (sample JBP-71-21) from the basal mylonitic band in the Sobrado Upper tectonic slice. (a) Hornblende-plagioclase mixtures and titanite with preferred orientation, defining the mylonitic fabric. (b) Main fabric surrounding a garnet porfiroclast. Note titanite is the Ti phase in the mylonitic fabric but ilmenite grains have been preserved inside the garnet. The position of (c) is indicated by a white dashed square. (c) Garnet inclusions from (b) where ilmenite inclusions show a progressive breakdown into titanite (Ilm>Ttn). Note ilmenite inclusions inside pristinte garnet areas show no evidence of transformation. (d) Inclusions of rutile inside titanite and partial transformation of plagioclase into zoisite. All micrographs in plane-polarized light (PPL). (Mineral abbreviations after Whitney and Evans, 2010; Hbl: hornblende, Ttn: titanite, Ilm: ilmenite, Rt: rutile, Pl: plagioclase, Zo: zoisite, Grt: garnet).

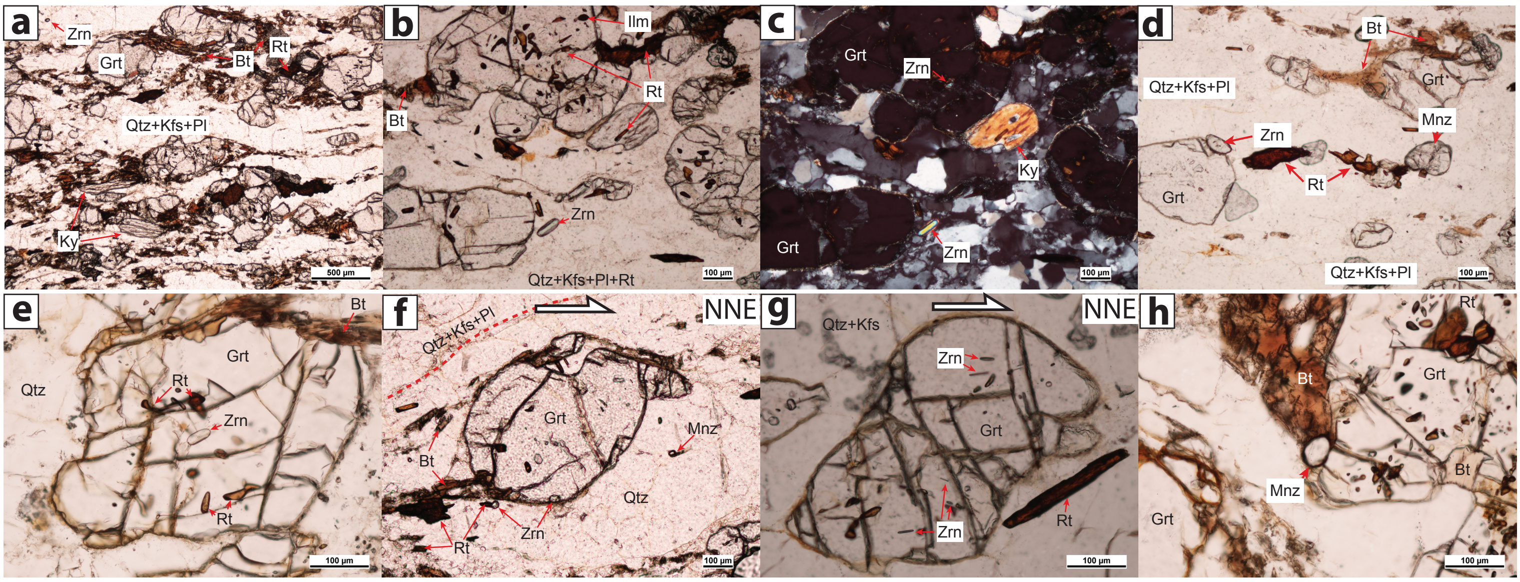

Figure 4. Granulite facies migmatitic paragneiss from the Sobrado Middle horse (Fig. 2). (a) General microstructure where leucosome bands and preferred orientation of elongated garnets, biotite, rutile and kyanite define the foliation. (b) Zircon elongated grain in recrystallized leucosome domain. Main inclusions in garnet include rutile, ilmenite and zircon (PPL) and (c) Cross-polarized ligth (CPL). (d) Monazite and zircon subrounded grain in the leucosome domain. (e) Subrounded elongated grain of zircon included in a garnet. (f) Plastically deformed garnet (sigmoidal grain) in a leucosome. Zircon and monazite are found in the quartz-rich area around the garnet. (g) Sigmoidal garnet in a leucosome. Inclusions of prismatic and bipiramidal zircons and rutile are observed. (h) Monazite grain in a garnet pressure shadow with biotite. Ky: kyanite, Bt: biotite, Qtz: quartz, Kfs: K-felspard, Pl: plagioclase, Rt: rutile, Zrn: zircon, Mnz: monazite, Grt: garnet.

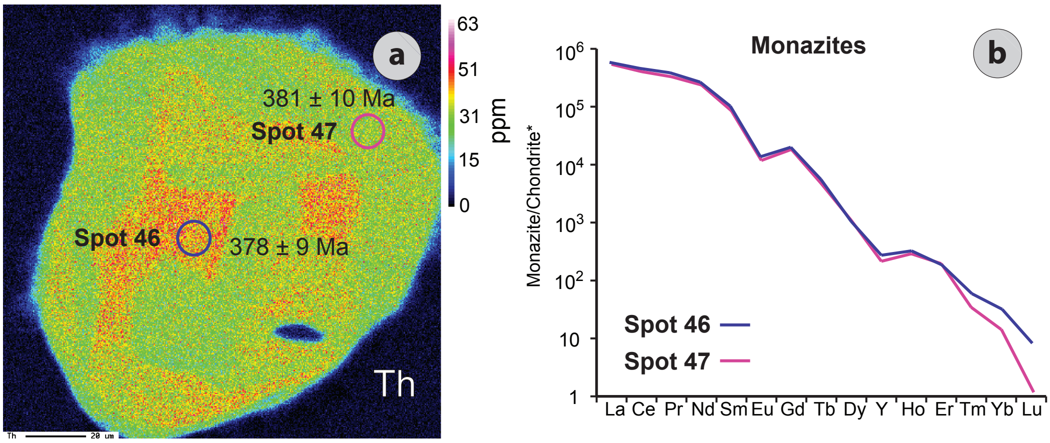

Figure 5. (a) Monazite grain compositional maps in paragneiss with a 30% thorium variation. Location and spot numbers (46 and 47) are indicated, as well as the $^{206}Pb/^{238}U$ age and error (±2σ). (b) Chondrite-normalized rare earth element (REE) patterns for the same monazites in (a).

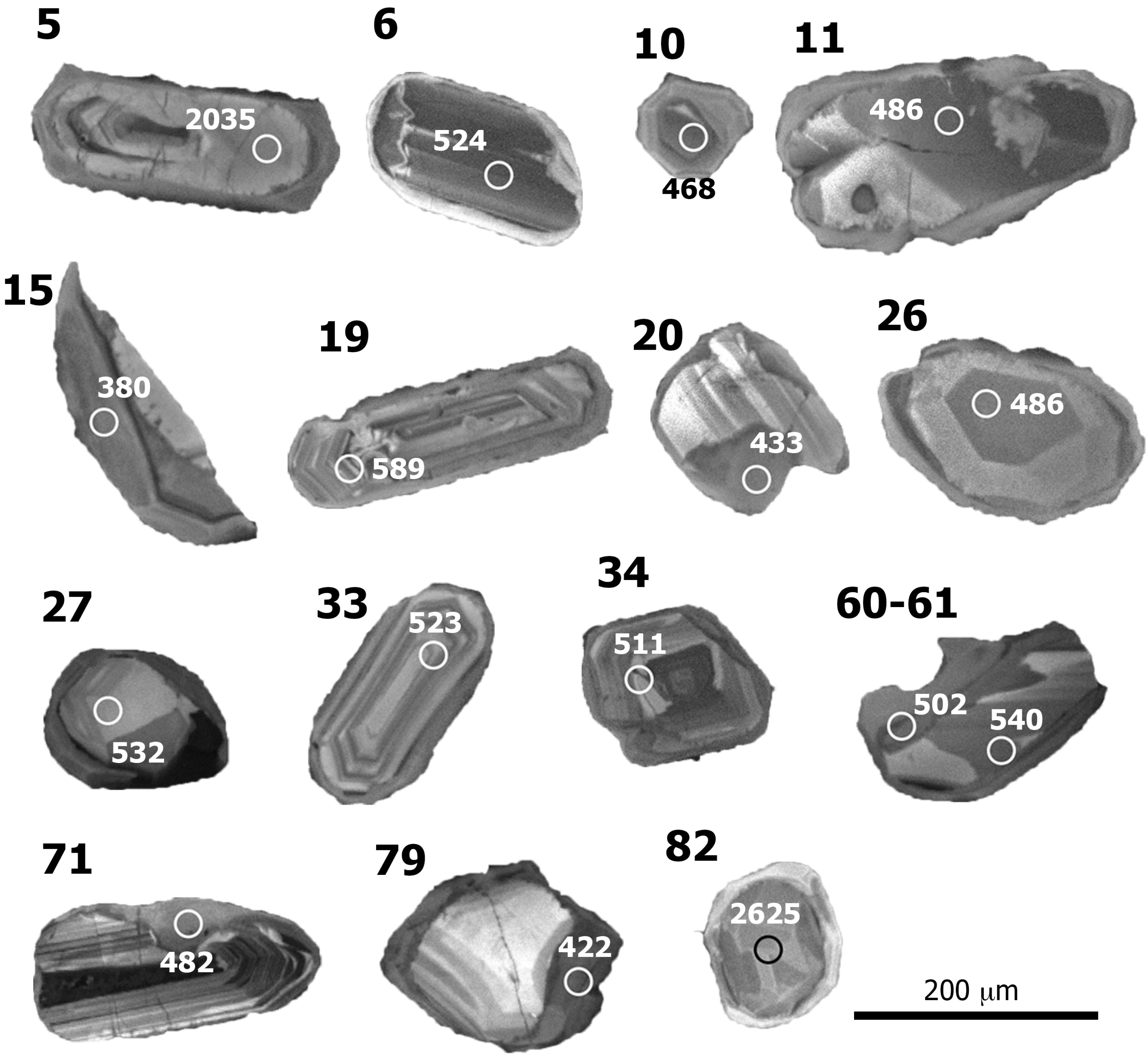

Figure 6: Cathodoluminescence (CL) images with the location of the analyzed spots for selected zircon grains.

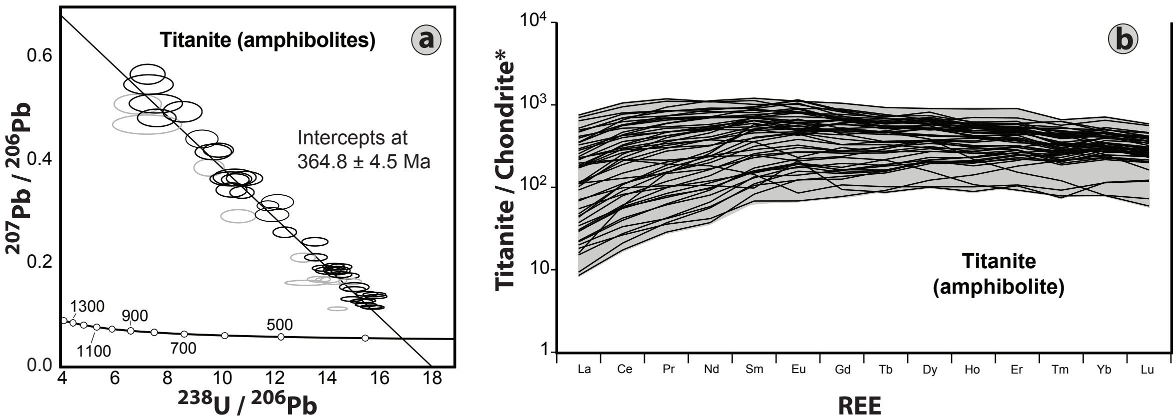

Figure 7. (a) Tera-Wasserburg diagram showing distribution of analyzed titanites (n = 51) from Sobrado amphibolite (JBP-71-21). The rejected analyses are represented by gray ellipses. The ellipses represent the $^{207}Pb/^{206}Pb$ and $^{238}U/^{206}Pb$ errors (±2σ). (b) Chondrite-normalized rare earth element (REE) patterns for the same titanites.

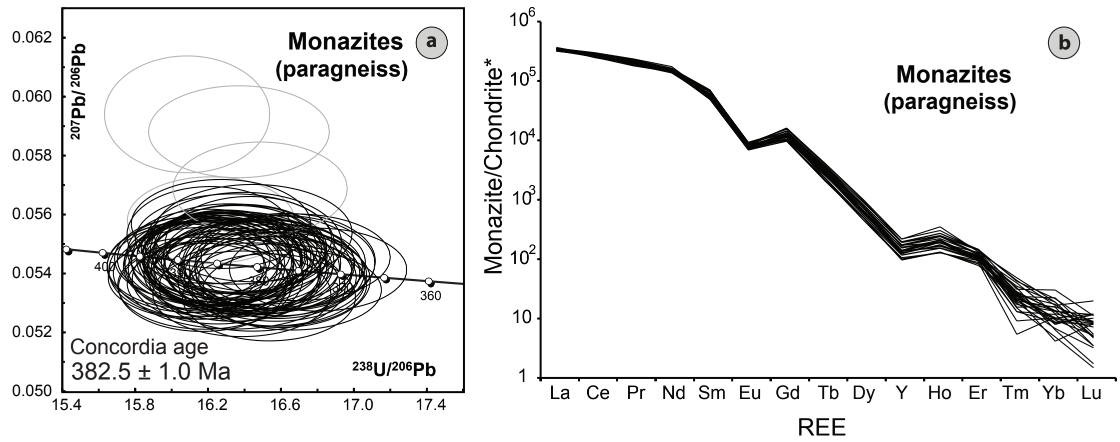

Figure 8. (a) Tera-Wasserburg diagram showing distribution of analyzed monazites (n = 76) from Sobrado paragneiss (*JBP-71-15*). The rejected analyses are represented by gray ellipses. The ellipses represent the $^{207}Pb/^{206}Pb$ and $^{238}U/^{206}Pb$ errors (±2σ). (b) Chondrite-normalized rare earth element (REE) patterns for the same monazites.

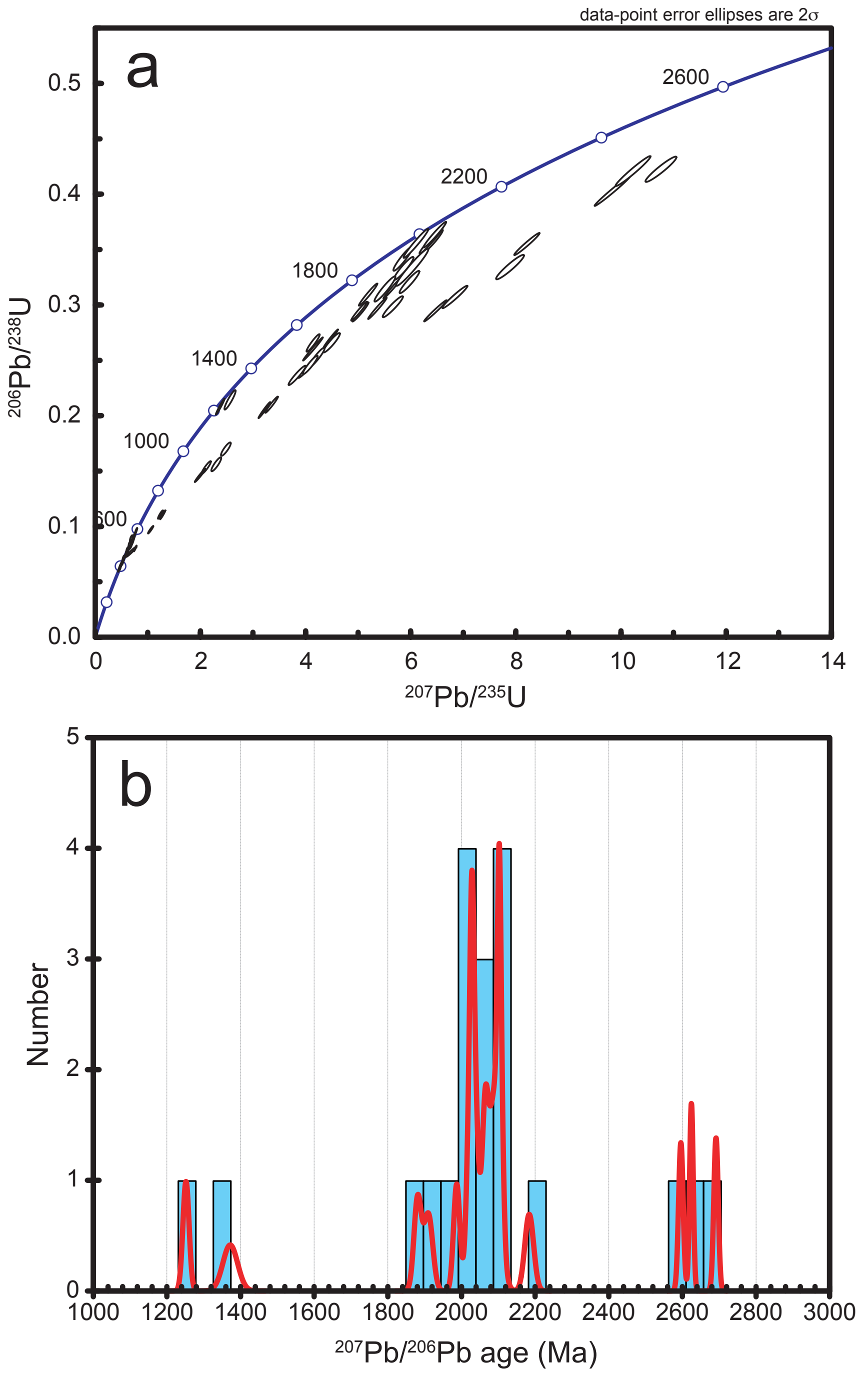

Figure 9: Concordia plot (a) including all zircon with concordance >90% from sample JBP-71-15 (Sobrado migmatitic paragneiss), and (b) age histogram and probability density plot for ages older than 1000 Ma.

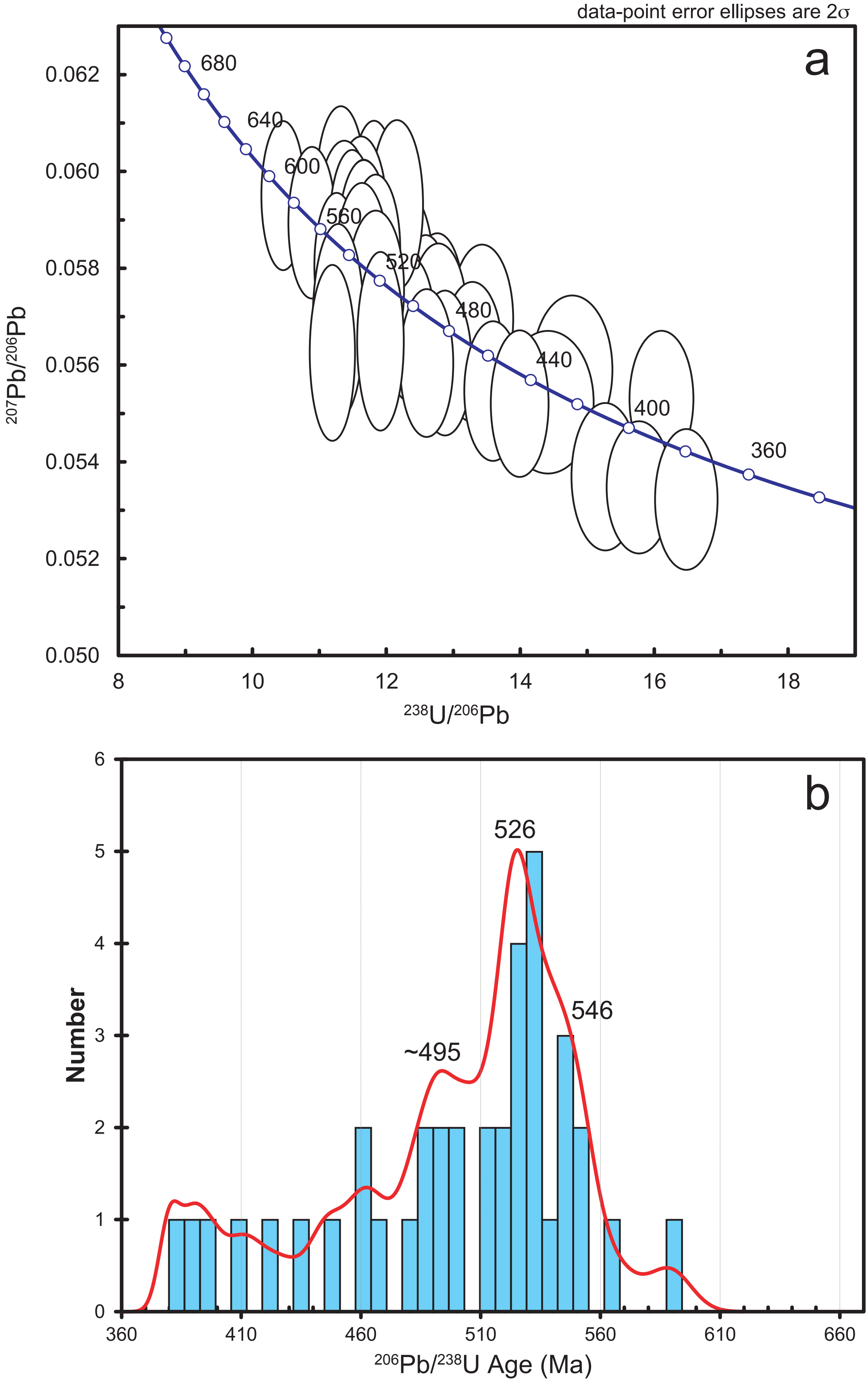

Figure 10: Tera-Wasserburg diagram (a) for the analyses between 589 and 380 Ma, and, (b) age histogram and probability density plot for the same ages.

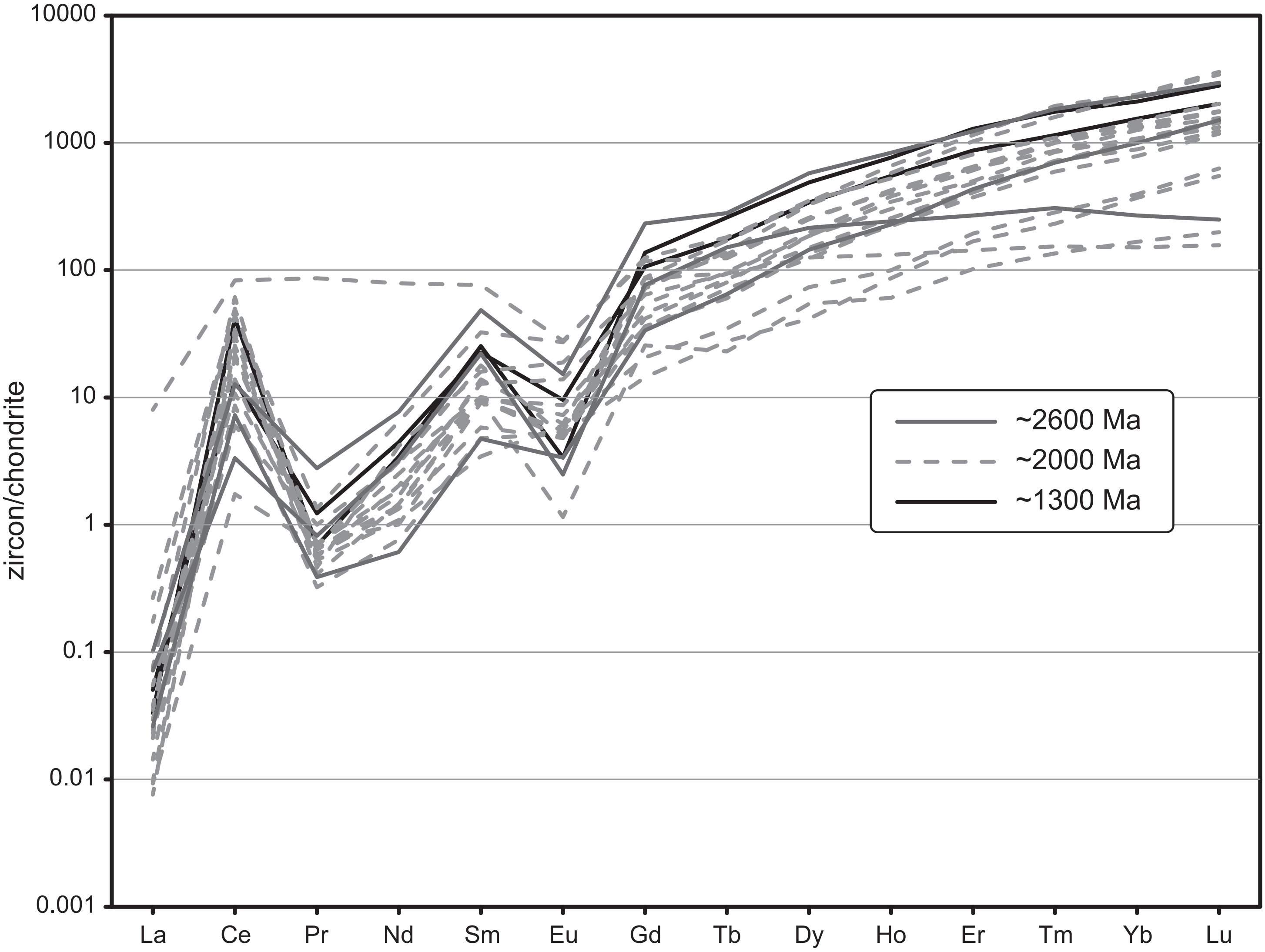

Figure 11: Chondrite-normalized plots for inherited zircon older than 1000 Ma.

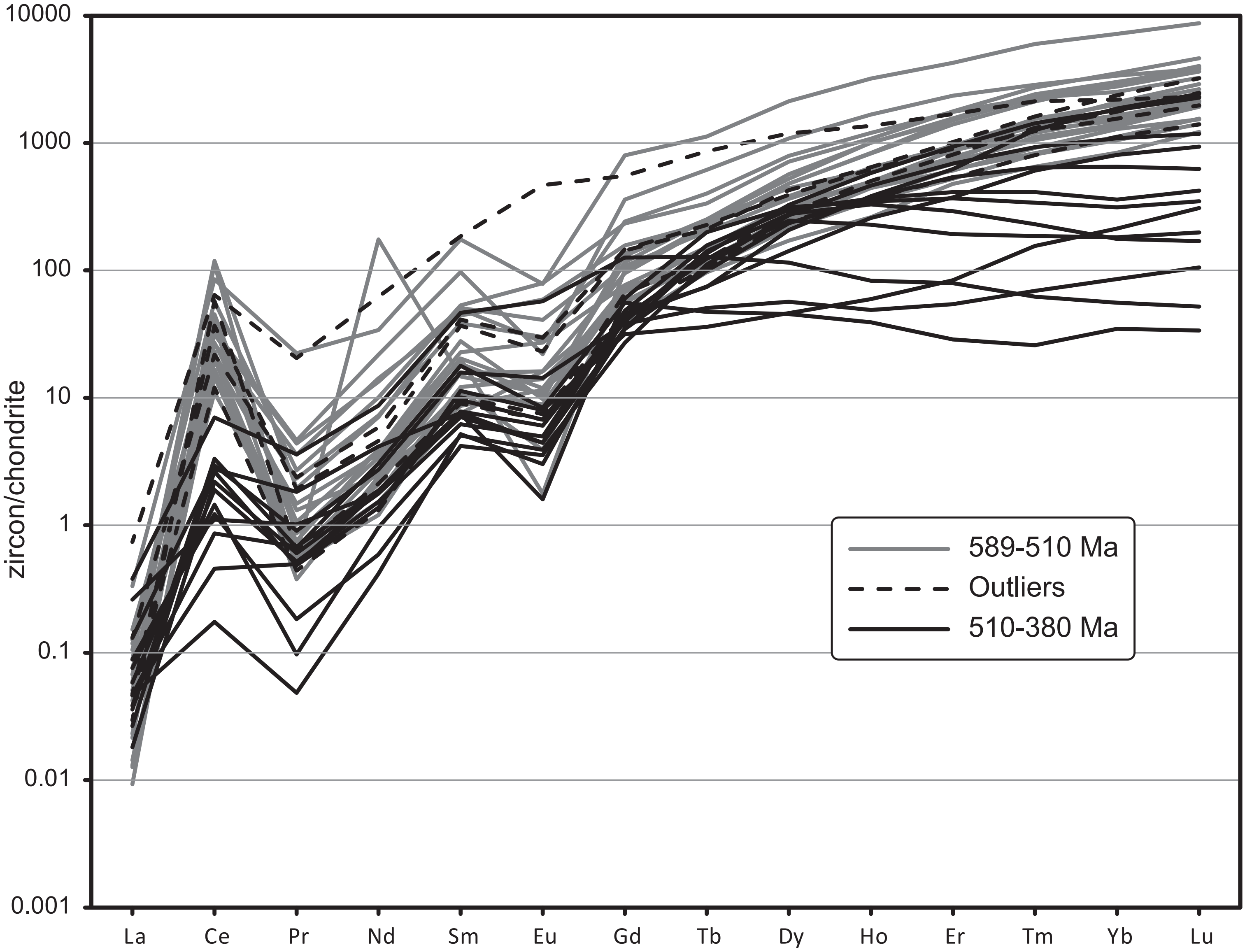

Figure 12: Chondrite-normalized plots for zircon between 589 and 380 Ma.

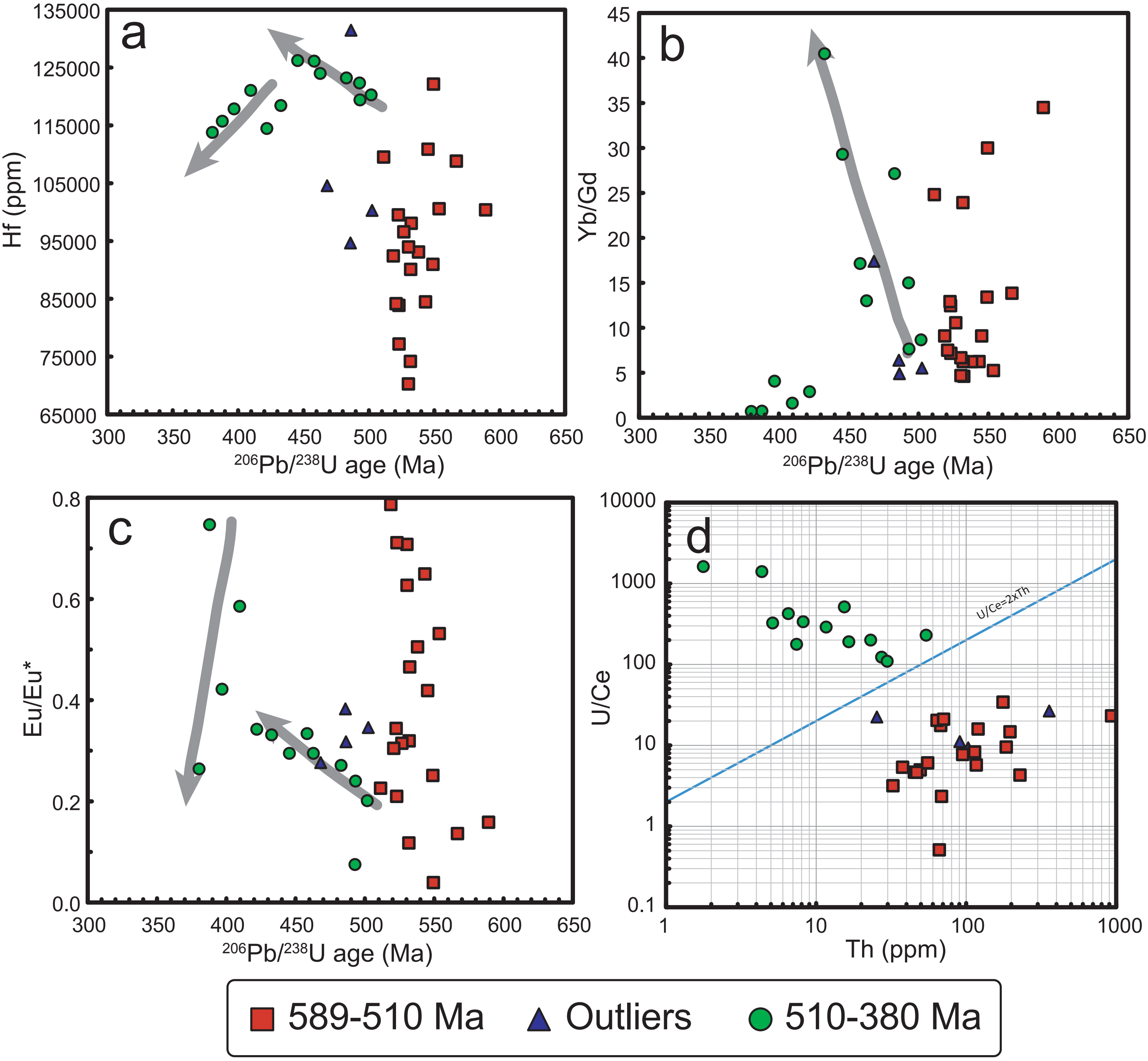

Figure 13: (a) Hafnium versus age, (b) Yb/Gd versus age, (c) Eu/Eu* versus age, and (d) U/Ce versus Th for zircon analyses between 589 and 380 Ma.

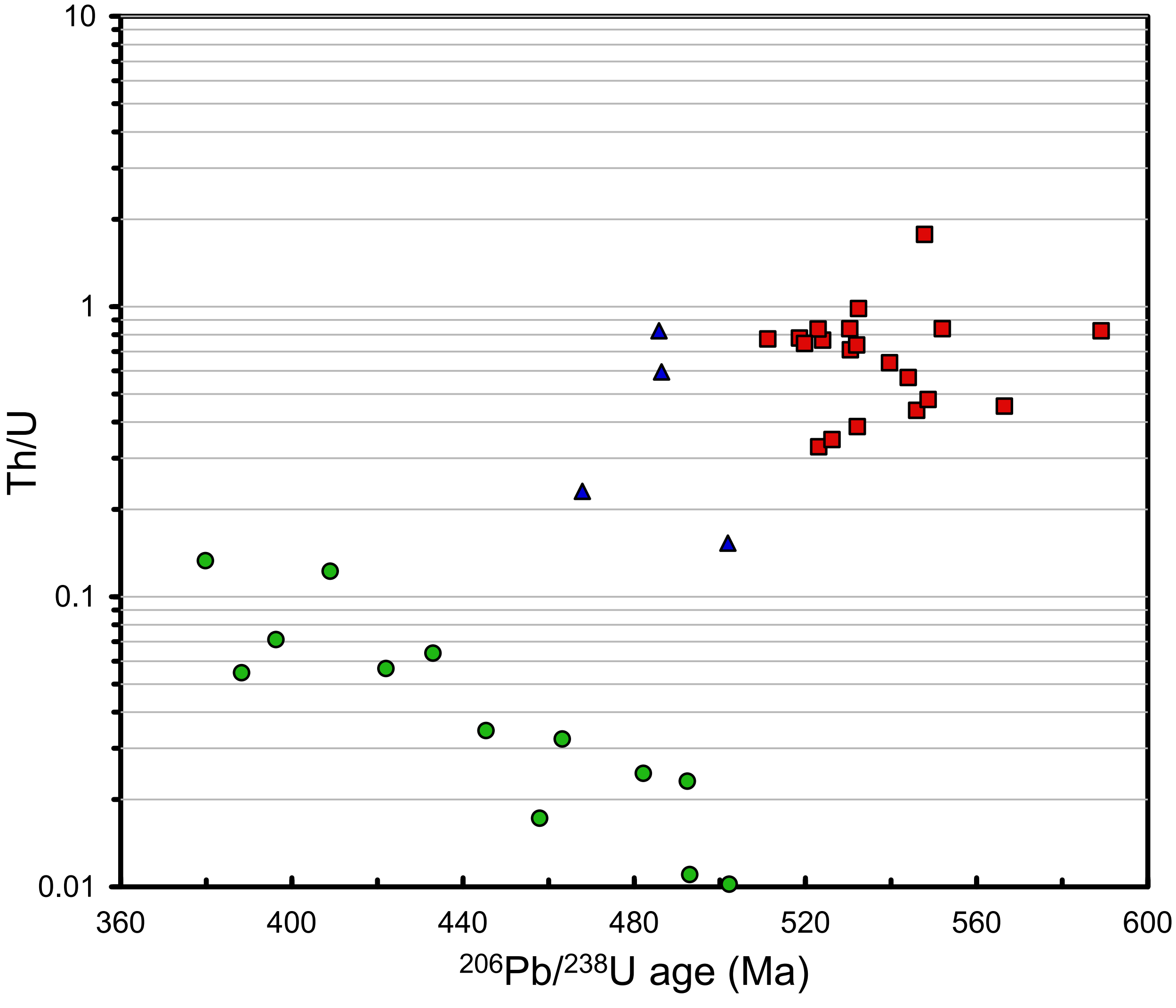

Figure 14:Th/U ratio versus $^{206}Pb/^{238}U$ ages for the zircon analyses from 589 to 380 Ma. Analysis 63 (510 Ma) is not represented as it has an anomalous value (6.59).

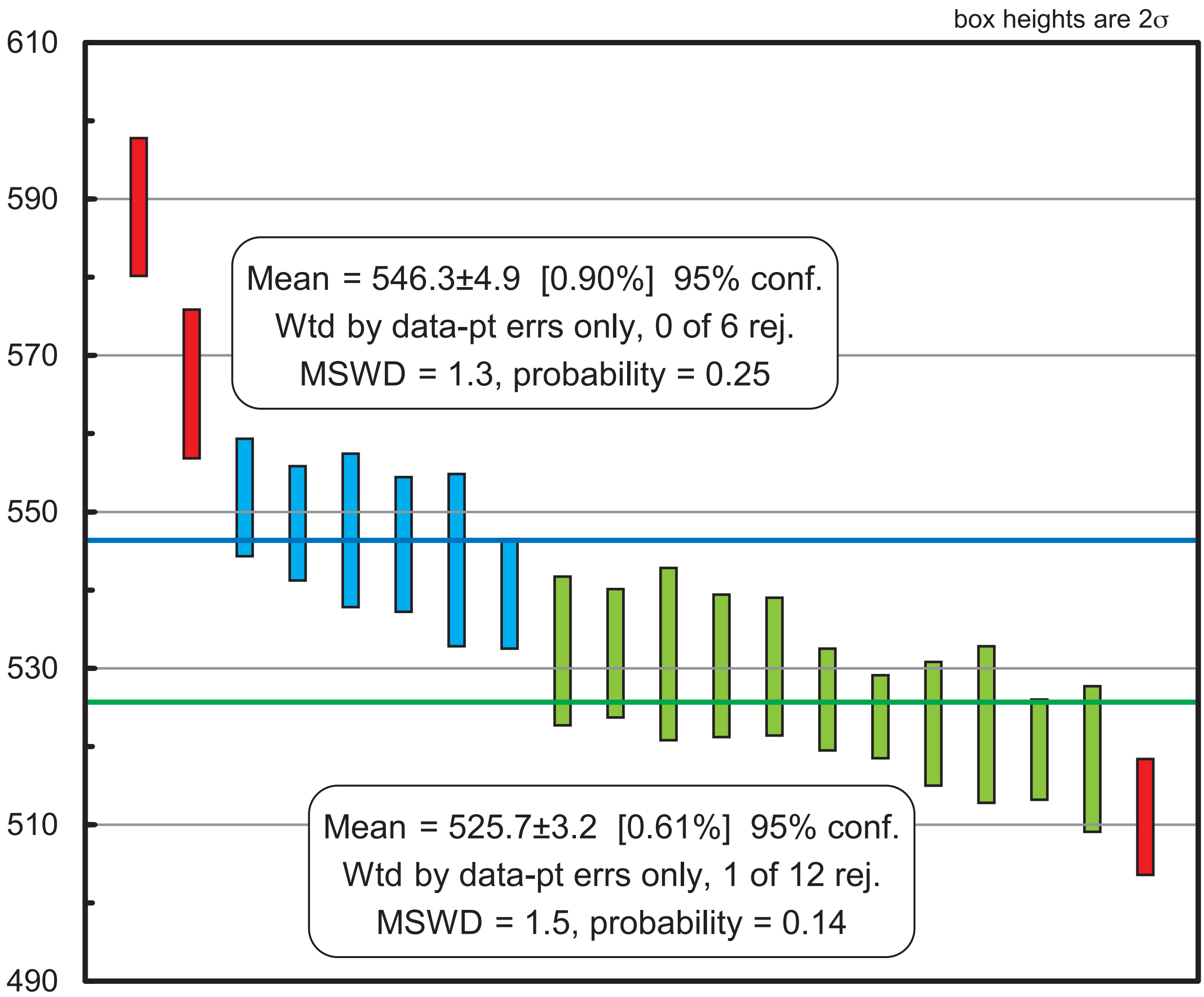

Figure 15:Weigthed average obtained from magmatic ages distributed between 589 and 510 Ma.

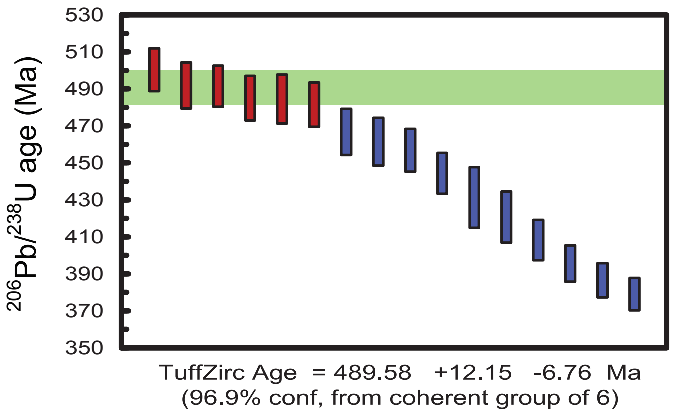

Figure 16: Age of the onset of the oldest HP-HT metamorphic event obtained using the TuffZirc algorythm.

Table 1_U-Th_Pb+REE Titatine_McD_s

Spot	$^{238}U/^{206}Pb$		$^{207}Pb/^{206}Pb$		$^{208}Pb/^{232}Th$		U (ppm)	Th (ppm)	La (ppm)	Ce (ppm)	Pr (ppm)	Nd (ppm)	Sm (ppm)	Eu (ppm)	Gd (ppm)	Tb (ppm)	Dy (ppm)	Ho (ppm)	Er (ppm)	Tm (ppm)	Yb (ppm)	Lu (ppm)
1	15.59	± 0.35	0.1279	± 0.0032	0.02292	± 0.00053	7.42	16.57	751	1052	1182	1096	1012	1012	818	681	635	590	521	423.1	405	363.4
2	13.37	± 0.66	0.1625	± 0.0040	0.02580	± 0.00074	8.22	16.73	701	946	1107	1085	1128	904	889	762	661	584	483	333.6	324	232.9
3	13.74	± 0.36	0.2123	± 0.0056	0.03513	± 0.00101	4.16	7.44	327	424	520	538	650	588	574	559	522	538	532	411.7	465	392.7
4	13.85	± 0.36	0.1694	± 0.0045	0.05140	± 0.00298	4.30	2.47	116	188	275	318	484	519	503	471	419	408	365	278.9	299	230.5
5	13.70	± 0.41	0.2426	± 0.0067	0.05450	± 0.00376	2.71	2.35	109	209	297	383	511	561	458	437	422	416	386	287.9	315	261.4
6	14.20	± 0.40	0.1864	± 0.0058	0.03180	± 0.00119	3.16	4.74	225	300	369	409	547	671	515	539	495	526	511	393.5	448	383.7
7	12.06	± 0.52	0.2955	± 0.0111	0.15000	± 0.18002	2.00	1.46	68	111	153	199	314	382	329	361	373	394	399	318.6	340	290.7
8	14.52	± 0.33	0.1863	± 0.0050	0.03051	± 0.00091	4.86	7.93	394	574	681	705	762	813	685	648	589	608	579	436.8	504	417.1
9	15.11	± 0.35	0.1310	± 0.0037	0.02719	± 0.00074	6.55	10.39	471	692	733	803	861	828	714	679	636	703	693	565.6	650	561.0
10	12.55	± 0.37	0.2611	± 0.0083	0.14400	± 0.04010	2.35	0.96	45	90	152	217	359	442	328	329	300	291	304	252.6	290	245.5
11	15.48	± 0.35	0.1264	± 0.0034	0.03340	± 0.00137	8.13	6.22	350	654	938	1120	1201	1107	1045	928	902	890	901	659.9	711	586.6
12	7.30	± 1.08	0.4710	± 0.0153	0.07200	± 0.09601	0.61	0.32	15	27	42	67	134	140	162	189	215	233	264	248.2	287	232.1
13	10.02	± 0.47	0.4211	± 0.0111	0.11200	± 0.09503	1.20	0.69	31	61	98	139	244	209	230	214	156	108	93	78.5	80	72.8
14	9.66	± 0.47	0.3870	± 0.0135	0.22000	± 0.17006	1.09	0.56	29	55	79	96	159	197	160	181	200	213	249	230.4	296	242.7
15	13.99	± 0.32	0.1910	± 0.0046	0.03377	± 0.00107	4.58	6.10	184	317	421	512	599	485	518	467	433	401	374	319.8	306	236.2
16	14.41	± 0.41	0.1672	± 0.0063	0.03150	± 0.00144	4.02	5.44	216	359	421	492	642	501	609	609	590	549	545	471.3	464	395.9
17	14.94	± 0.36	0.1761	± 0.0048	0.13000	± 0.03609	4.38	0.71	43	108	170	239	404	460	433	485	572	540	536	488.3	420	339.0
18	7.35	± 0.77	0.5490	± 0.0155	-0.08000	± -0.14001	0.55	0.30	18	26	36	42	68	68	77	92	122	141	181	210.9	230	204.5
19	15.96	± 0.36	0.1397	± 0.0034	0.02710	± 0.00071	8.10	9.22	414	520	541	580	692	609	652	624	708	579	591	630.8	507	405.7
20	15.04	± 0.36	0.1649	± 0.0049	0.03031	± 0.00096	6.39	8.79	293	426	468	522	543	499	482	455	514	419	438	446.6	412	321.1
21	11.90	± 0.34	0.3127	± 0.0079	0.37000	± 0.22012	2.91	0.40	48	108	185	276	507	426	527	465	385	218	153	120.2	80	59.3
22	14.41	± 0.34	0.1940	± 0.0054	0.05140	± 0.00216	5.29	3.73	255	465	598	716	889	794	766	709	817	603	595	629.1	472	382.1
23	14.18	± 0.37	0.1682	± 0.0046	0.09800	± 0.01612	4.77	1.43	102	228	355	458	710	718	687	604	671	488	476	449.4	344	258.5
24	15.92	± 0.35	0.1147	± 0.0030	0.02388	± 0.00057	10.78	13.20	468	695	829	915	901	1052	731	604	620	458	442	428.3	323	278.0
25	7.63	± 0.83	0.5120	± 0.0150	-0.03000	± -0.49000	0.68	0.14	9	21	37	56	110	157	147	157	209	182	211	270.4	234	214.2
26	12.27	± 0.50	0.3200	± 0.0119	0.05770	± 0.00542	1.68	2.17	93	148	203	243	286	325	275	274	313	271	307	349.0	312	285.4
27	14.67	± 0.35	0.1937	± 0.0048	0.03279	± 0.00098	4.67	6.77	354	560	653	700	703	639	652	551	557	401	347	332.8	248	162.6
28	15.20	± 0.46	0.1543	± 0.0069	0.03350	± 0.00183	4.88	4.43	174	326	463	554	642	542	593	512	581	487	521	521.1	496	453.7
29	14.56	± 0.31	0.1120	± 0.0029	0.02158	± 0.00049	11.71	22.45	495	625	696	722	728	886	653	584	642	562	575	536.0	444	363.0
30	10.92	± 0.38	0.3387	± 0.0094	0.05840	± 0.00378	1.54	2.51	111	129	147	168	229	267	270	312	375	364	431	455.9	451	411.0
31	10.64	± 0.67	0.3680	± 0.0132	0.12200	± 0.03409	1.07	0.81	29	58	84	114	158	173	195	184	230	228	262	283.0	270	259.3
32	9.39	± 0.50	0.4430	± 0.0141	-0.02000	± -0.12000	0.90	0.58	22	42	61	81	130	179	152	162	207	205	242	246.2	289	248.8
33	10.49	± 0.65	0.3651	± 0.0111	0.09500	± 0.00969	1.13	1.22	55	82	100	120	149	189	163	162	203	196	229	210.5	247	236.6
34	15.19	± 0.35	0.1501	± 0.0040	0.04200	± 0.00163	5.56	3.48	235	434	593	696	705	801	639	537	517	454	488	390.3	419	399.2
35	14.53	± 0.41	0.1866	± 0.0067	0.03390	± 0.00129	3.69	4.89	172	263	322	383	457	471	483	465	516	482	494	401.6	464	401.2
36	14.66	± 0.36	0.1785	± 0.0047	0.05840	± 0.00378	4.36	2.21	111	252	399	514	703	588	649	544	524	463	461	351.8	391	368.3
37	16.03	± 0.34	0.1359	± 0.0032	0.04720	± 0.00230	8.41	3.38	281	400	473	503	493	611	443	355	366	321	320	264.8	297	287.8
38	10.52	± 0.48	0.3435	± 0.0113	0.14400	± 0.06906	1.28	0.55	22	40	63	93	172	221	236	293	370	352	385	304.0	348	308.1
39	8.65	± 0.61	0.4960	± 0.0164	0.00000	± 0.00000	0.66	0.24	9	17	29	37	83	123	126	158	215	232	284	215.8	278	267.9
40	15.85	± 0.34	0.1160	± 0.0028	0.02681	± 0.00080	7.59	7.20	348	566	735	869	950	1151	862	731	739	619	632	420.2	530	460.6
41	11.89	± 0.31	0.1654	± 0.0046	0.06000	± 0.14001	2.54	0.09	16	60	148	259	580	512	585	518	511	425	428	291.9	411	362.2
42	9.82	± 0.57	0.4175	± 0.0124	0.13800	± 0.08205	0.95	0.79	71	99	105	105	98	210	94	87	100	89	104	74.5	115	122.0
43	15.67	± 0.34	0.1411	± 0.0037	0.02576	± 0.00068	6.21	10.38	640	799	852	832	803	913	671	607	625	520	493	319.8	397	362.2
44	11.01	± 0.57	0.3661	± 0.0111	0.11000	± 0.14002	1.20	0.86	34	57	75	99	154	196	174	218	270	274	316	272.5	369	345.9
45	7.67	± 0.60	0.4840	± 0.0139	0.04000	± 0.25000	0.57	0.33	20	33	42	58	105	123	136	150	193	200	221	204.0	263	280.5
46	13.25	± 0.39	0.2117	± 0.0071	0.03790	± 0.00242	2.61	4.41	228	284	304	324	395	455	384	348	358	302	284	195.5	227	204.9
47	10.78	± 0.54	0.2924	± 0.0105	0.13300	± 0.07405	1.66	0.79	37	79	118	165	255	304	277	309	340	313	321	253.8	305	288.2
48	6.94	± 0.74	0.5110	± 0.0158	0.07450	± 0.00570	0.64	1.89	173	290	339	376	356	230	303	269	273	260	255	186.6	217	199.2
49	15.64	± 0.33	0.1197	± 0.0028	0.03214	± 0.00100	10.32	7.50	521	772	845	886	937	1130	839	676	683	551	478	336.0	339	299.2
50	10.66	± 0.43	0.3635	± 0.0094	0.06970	± 0.00481	1.77	2.45	197	218	213	235	245	269	259	261	294	258	279	210.9	246	236.6
51	7.32	± 0.55	0.5690	± 0.0158	0.08940	± 0.00820	0.70	1.76	183	217	191	182	143	85	107	102	102	101	107	92.3	114	118.7

Table 2A_U-Th_Pb+REE Monazite _McD_S

Spot	$^{238}U/^{206}Pb$	±	$^{207}Pb/^{206}Pb$	±	$^{208}Pb/^{232}Th$	±	U (ppm)	Th (ppm)	La (ppm)	Ce (ppm)	Pr (ppm)	Nd (ppm)	Sm (ppm)	Eu (ppm)	Gd (ppm)	Tb (ppm)	Dy (ppm)	Y (ppm)	Ho (ppm)	Er (ppm)	Tm (ppm)	Yb (ppm)	Lu (ppm)
1	16.29	± 0.35	0.0543	± 0.0013	0.01930	± 0.00041	1640	26200	554430	433931	365302	243982	98243	12131	19899	4429	992	243	273	170	32.4	20	3.3
2	16.28	± 0.35	0.0545	± 0.0013	0.01916	± 0.00042	1850	29300	527004	437194	352371	242451	94324	13286	19749	4490	1081	272	322	191	27.5	25	0.0
3	16.20	± 0.38	0.0544	± 0.0012	0.01949	± 0.00044	2300	25500	519409	420881	346983	250109	107905	12451	23869	5319	1163	282	374	190	71.7	8	24.8
4	16.30	± 0.38	0.0546	± 0.0013	0.01930	± 0.00047	1454	34200	563713	425775	323276	223632	85270	11474	18543	4266	898	192	251	118	46.6	6	12.2
5	16.18	± 0.36	0.0543	± 0.0012	0.01926	± 0.00043	1805	32400	547257	420881	353448	231947	92568	11385	19899	4197	959	179	260	143	38.1	14	0.0
6	16.09	± 0.35	0.0541	± 0.0013	0.01946	± 0.00044	1660	25900	524051	409462	338362	238074	96622	11794	19045	4634	980	227	291	184	44.5	19	5.7
7	16.27	± 0.36	0.0544	± 0.0012	0.01938	± 0.00045	1790	29000	554430	442088	369612	230853	95676	12647	19598	4072	1045	248	310	172	46.6	20	30.5
8	16.15	± 0.36	0.0545	± 0.0012	0.01920	± 0.00042	2170	44100	579325	437194	359914	248796	97838	13179	18693	3875	927	203	306	182	42.1	12	8.1
9	16.22	± 0.37	0.0558	± 0.0012	0.01900	± 0.00043	2150	47100	567511	422512	340517	245295	90608	12451	17789	3958	902	232	286	179	52.2	6	25.6
10	16.38	± 0.38	0.0549	± 0.0012	0.01940	± 0.00045	1680	27900	526160	435563	357759	242451	93919	12664	19799	4078	947	210	264	143	46.2	11	8.9
11	16.20	± 0.37	0.0547	± 0.0012	0.01930	± 0.00044	1950	35700	555274	433931	383621	254923	95270	12060	19296	4432	996	221	321	181	44.1	17	5.7
12	16.29	± 0.37	0.0546	± 0.0012	0.01915	± 0.00044	2280	32800	555274	415987	336207	252298	103176	13215	20201	4510	976	236	280	195	39.7	7	0.0
13	16.35	± 0.38	0.0548	± 0.0012	0.01897	± 0.00044	2230	43200	540928	411093	349138	246827	94662	12202	18643	4551	976	218	282	138	36.0	13	0.0
14	16.28	± 0.36	0.0545	± 0.0012	0.01908	± 0.00043	2060	41000	564135	438825	362069	230197	95608	12575	19296	4269	866	209	251	162	16.2	13	11.8
15	16.31	± 0.39	0.0545	± 0.0012	0.01920	± 0.00045	2020	29600	535865	450245	378233	242888	109932	13268	22412	5125	1085	264	335	179	56.7	16	8.1
16	16.23	± 0.36	0.0544	± 0.0012	0.01953	± 0.00044	1714	31400	562447	460033	391164	261050	103514	13748	19196	4432	988	211	244	182	37.2	14	12.2
17	16.40	± 0.36	0.0546	± 0.0012	0.01910	± 0.00045	2360	37500	565401	429038	366379	241357	96689	12398	18894	4352	1004	218	291	177	25.5	10	8.9
18	16.22	± 0.36	0.0545	± 0.0012	0.01943	± 0.00043	1662	30800	580591	464927	376078	262363	100000	12256	18894	4654	1081	228	308	168	48.2	17	3.3
19	16.25	± 0.38	0.0538	± 0.0013	0.01932	± 0.00046	1600	31200	618143	442088	383621	244420	101419	12593	20050	4399	1024	217	253	161	34.0	4	2.8
20	16.11	± 0.35	0.0545	± 0.0012	0.01915	± 0.00042	2190	34200	567932	427406	364224	240919	101351	12611	19899	4598	1012	238	300	201	30.8	18	6.9
21	16.17	± 0.35	0.0543	± 0.0012	0.01926	± 0.00045	1804	28900	537975	443719	365302	243326	100608	13428	18693	4197	951	208	286	153	39.7	17	3.3
22	16.08	± 0.35	0.0543	± 0.0012	0.01964	± 0.00044	2380	38200	560338	448613	383621	249672	101554	12913	19497	5125	1065	222	308	167	21.1	16	9.3
23	16.08	± 0.37	0.0594	± 0.0016	0.01886	± 0.00044	1704	84000	562447	391517	327586	231947	87635	12487	16281	4019	951	246	264	215	68.0	30	40.7
24	16.18	± 0.39	0.0536	± 0.0012	0.01938	± 0.00049	1650	29500	541772	417618	359914	238731	97230	12647	18693	4529	1110	246	315	188	31.2	19	11.0
25	16.37	± 0.39	0.0546	± 0.0012	0.01876	± 0.00045	1900	57800	564557	417618	337284	232604	94797	11634	16935	4030	894	217	295	148	79.4	12	3.7
26	16.43	± 0.38	0.0550	± 0.0013	0.01922	± 0.00044	1663	27800	566667	422512	360991	243545	97635	12700	17236	4488	963	249	288	184	56.3	8	14.6
27	16.32	± 0.39	0.0549	± 0.0012	0.01934	± 0.00049	2000	32900	575949	432300	354526	249453	100608	13250	19347	4958	1167	255	306	177	47.8	17	7.3
28	16.35	± 0.38	0.0538	± 0.0011	0.01948	± 0.00046	3680	28300	582700	445351	363147	264770	118243	15062	25025	6648	1553	383	443	213	45.7	25	16.7
29	16.58	± 0.35	0.0539	± 0.0011	0.01908	± 0.00044	3050	32100	551899	432300	385776	240044	118243	14512	24171	6427	1451	352	399	221	43.3	16	7.7
30	16.27	± 0.38	0.0546	± 0.0012	0.01941	± 0.00046	1822	27600	562447	440457	375000	260394	104054	13694	21156	5235	1102	240	332	191	30.4	24	16.7
31	16.63	± 0.40	0.0544	± 0.0013	0.01874	± 0.00045	1926	28200	570042	437194	350216	232604	99324	11261	18693	4432	992	211	288	196	51.8	18	3.3
32	16.68	± 0.42	0.0546	± 0.0012	0.01915	± 0.00047	2130	35500	542194	419250	371767	248359	102703	13144	18191	4834	996	243	291	168	47.8	21	0.0
33	16.36	± 0.37	0.0541	± 0.0012	0.01936	± 0.00044	2220	29500	556540	414356	369612	257987	100338	13197	20402	4709	1053	248	300	174	39.3	8	13.4
34	16.42	± 0.39	0.0544	± 0.0012	0.01944	± 0.00047	1950	30300	587342	407830	355603	255580	100000	12824	19648	4598	1041	253	289	166	21.9	16	18.3
35	16.39	± 0.41	0.0542	± 0.0012	0.01944	± 0.00050	2480	32400	562025	412724	367457	245514	113446	14725	24372	6427	1439	341	452	231	64.4	16	24.8
36	16.31	± 0.36	0.0544	± 0.0013	0.01912	± 0.00041	2010	43900	580591	402936	355603	258425	90405	10533	16935	4460	850	208	242	168	49.4	3	3.3
37	16.34	± 0.44	0.0552	± 0.0013	0.01948	± 0.00050	2200	42200	582700	435563	365302	247046	100811	13002	21809	5512	1150	239	295	179	33.2	35	9.3
38	16.54	± 0.38	0.0543	± 0.0012	0.01913	± 0.00049	2148	44200	571308	414356	363147	241794	92770	11829	18543	4645	1008	214	286	162	49.4	24	8.9
39	16.39	± 0.44	0.0550	± 0.0014	0.01960	± 0.00053	1419	32800	565823	443719	365302	249234	91014	11901	16935	4598	907	222	267	157	51.8	22	6.1
40	16.44	± 0.39	0.0542	± 0.0013	0.01949	± 0.00047	1930	31600	556540	424144	382543	257112	96757	12504	19598	4903	1175	256	326	203	45.3	17	20.7
41	16.37	± 0.38	0.0548	± 0.0012	0.01928	± 0.00044	1690	40600	562447	435563	387931	262363	85405	11332	18342	4571	1045	239	333	178	41.3	28	13.4
42	16.56	± 0.41	0.0544	± 0.0013	0.01950	± 0.00050	1655	34400	573418	420881	350216	243107	92095	12131	19246	4654	1037	231	321	164	27.9	12	0.0
43	16.26	± 0.37	0.0545	± 0.0013	0.01927	± 0.00044	2490	37200	569198	432300	383621	245952	88108	10728	18291	4211	915	204	286	164	21.5	16	13.8
44	16.33	± 0.40	0.0540	± 0.0012	0.01942	± 0.00047	2260	30300	585654	437194	376078	267396	95338	14369	19950	4737	1089	232	300	160	49.4	9	8.5
45	16.22	± 0.37	0.0542	± 0.0013	0.01942	± 0.00045	1600	44700	528692	414356	329741	239168	87365	10906	18945	4820	1057	245	326	183	11.7	23	0.0
46	16.57	± 0.41	0.0539	± 0.0013	0.01907	± 0.00049	1674	39800	538397	402936	328664	237199	85135	11812	18342	4681	1089	215	289	195	34.4	14	0.0
47	16.44	± 0.42	0.0535	± 0.0012	0.01927	± 0.00048	1920	30300	528692	417618	351293	243326	94054	12771	18593	5208	1000	262	311	180	57.5	31	8.1
48	16.39	± 0.40	0.0533	± 0.0012	0.01936	± 0.00049	1789	31400	540928	446982	350216	240263	89189	12220	17538	4349	898	202	317	151	21.5	19	5.7
49	16.21	± 0.37	0.0553	± 0.0013	0.01947	± 0.00046	1810	35800	570464	430669	375000	262582	99459	12824	21859	5125	1264	283	308	190	24.7	8	2.4

Table 2B_U-Th_Pb+REE Monazite _McD_S

Spot	$^{238}U/^{206}Pb$	±	$^{207}Pb/^{206}Pb$	±	$^{208}Pb/^{232}Th$	±	U (ppm)	Th (ppm)	La (ppm)	Ce (ppm)	Pr (ppm)	Nd (ppm)	Sm (ppm)	Eu (ppm)	Gd (ppm)	Tb (ppm)	Dy (ppm)	Y (ppm)	Ho (ppm)	Er (ppm)	Tm (ppm)	Yb (ppm)	Lu (ppm)
50	16.40	0.37	0.0543	0.0012	0.01944	0.00045	2020	31600	561603	411093	340517	233479	92838	12131	19196	4598	1000	219	337	168	21.5	14	16.7
51	16.66	0.40	0.0534	0.0011	0.01944	0.00047	4730	33200	523207	432300	303879	243545	110135	14512	25879	6759	1650	358	575	217	79.8	31	7.7
52	16.54	0.40	0.0540	0.00122	0.01953	0.000469	1900	36500	585654	474715	359914	258425	111283.8	14547	21859	5983	1341	318	410	239	69.6	35.4	13.4
53	16.61	0.42	0.0544	0.00132	0.01891	0.000502	1596	66200	545992	412398	295259	233260	84932.43	11758	18593	4391	1085	255	308	212	30.0	11.2	5.3
54	16.49	0.39	0.0569	0.00129	0.01916	0.000475	1611	57800	542616	437194	352371	244201	100202.7	13499	20804	4931	1081	232	350	159	36.4	21.7	8.1
55	16.34	0.48	0.0537	0.00125	0.01950	0.000545	1760	30200	581013	476346	371767	246827	94729.73	13357	19899	4377	1024	193	251	169	32.8	25.5	5.7
56	16.80	0.40	0.0541	0.00115	0.01912	0.000446	2240	37600	536709	438825	335129	235449	84797.3	11758	16985	4177	996	204	288	164	40.9	28.6	8.1
57	16.49	0.41	0.0540	0.00113	0.01979	0.000522	3610	30800	526160	461664	355603	247484	111621.6	13979	26533	6648	1602	318	447	240	51.0	49.7	18.3
58	16.33	0.40	0.0544	0.00121	0.01965	0.000471	2110	39100	568354	464927	329741	240700	80000	11279	16030	3767	748	165	216	128	38.9	16.8	0.0
59	16.59	0.38	0.0542	0.0012	0.01946	0.000442	3130	33400	556118	461664	344828	250985	93648.65	11883	19698	4873	976	222	271	173	42.9	13.0	19.5
60	16.59	0.38	0.0540	0.0012	0.01944	0.000447	3270	30600	567511	450245	322198	245733	111283.8	13854	23819	5956	1524	323	445	236	36.4	16.8	19.5
61	16.55	0.42	0.0537	0.00124	0.01905	0.00045	1860	69500	540928	433931	309267	224508	87702.7	12256	16683	3518	752	174	209	156	36.4	6.8	13.4
62	16.14	0.40	0.0538	0.00114	0.01945	0.000517	3700	34000	579325	481240	346983	233260	114189.2	14760	25226	6288	1467	359	498	232	72.1	27.3	32.5
63	16.35	0.38	0.0539	0.00121	0.01971	0.000462	2030	32300	582700	477977	342672	245733	94256.76	13464	18894	4343	967	227	255	166	38.9	36.6	8.9
64	16.45	0.44	0.0554	0.00135	0.01954	0.000525	1700	32600	584388	461664	345905	228665	100000	12398	22010	5457	1248	287	397	194	44.9	22.4	14.2
65	16.59	0.40	0.0538	0.00132	0.01921	0.00047	1476	33600	602532	453507	372845	246827	88648.65	12007	18794	4609	988	210	277	182	65.2	19.9	13.8
66	16.37	0.41	0.0588	0.00127	0.01931	0.000483	1900	42200	518987	451876	314655	231072	82297.3	12575	16432	3449	833	164	212	144	8.9	17.4	0.0
67	16.36	0.40	0.0541	0.00114	0.01942	0.000473	2520	30760	554008	451876	355603	263020	112702.7	15293	23266	5789	1362	313	401	203	46.6	21.7	19.1
68	16.58	0.40	0.0536	0.00114	0.01947	0.000486	4360	30500	551055	445351	365302	253611	106891.9	12895	21859	5180	1167	253	342	175	54.3	10.6	2.8
69	16.48	0.36	0.0544	0.00126	0.01949	0.000443	2458	38700	540506	474715	376078	270460	98175.68	12860	19598	4571	1020	230	319	166	40.5	14.3	13.0
70	16.53	0.39	0.0532	0.00121	0.01933	0.00046	2109	32100	576371	450408	367457	266521	106081.1	13606	20251	4535	1053	232	317	178	28.3	21.7	0.0
71	16.45	0.44	0.0542	0.0013	0.01924	0.00052	1890	47000	562447	438825	335129	252079	98310.81	12877	19246	4321	959	221	321	186	34.0	13.7	19.1
72	16.48	0.42	0.0544	0.00118	0.01953	0.000499	1660	34700	583966	491028	385776	286433	96013.51	13819	19749	4488	1179	283	364	203	44.5	15.5	8.5
73	16.27	0.40	0.0557	0.00123	0.01927	0.000501	1970	86900	597046	405057	315733	243107	80135.14	11545	15829	3399	813	159	214	136	31.6	16.1	11.8
74	16.18	0.41	0.0540	0.00127	0.01937	0.000484	2270	37100	594937	442088	334052	248578	89054.05	12078	18492	3853	833	192	251	157	15.0	16.8	13.4
75	16.17	0.38	0.0535	0.00122	0.01985	0.000459	2460	31100	580591	451876	365302	266740	116216.2	14174	23317	5568	1276	276	394	232	25.5	26.1	14.6
76	16.11	0.38	0.0542	0.00126	0.01946	0.000452	1563	33400	582278	446982	348060	269147	104729.7	14121	20251	4479	984	219	271	175	22.3	9.3	8.9

Table 3_U-Th_Pb Zircon sorted by age

Spot	Location	U (ppm)	Th (ppm)	Th/U	$^{207}Pb/^{235}U$	2σ	$^{206}Pb/^{238}U$	2σ	$^{207}Pb/^{206}Pb$	2σ	ρ	$^{207}Pb/^{235}U$ Age (Ma)	2σ	$^{206}Pb/^{238}U$ Age (Ma)	2σ	$^{207}Pb/^{206}Pb$ Age (Ma)	2σ	Probability of concordance
3	Core	690	223	0.32	10.760	0.242	0.423	0.0093	0.184	0.004	-0.05	2502	9	2272	18	2691	6	0.91
72		495	22	0.04	10.230	0.273	0.421	0.0111	0.174	0.004	0.06	2455	16	2264	33	2596	6	0.92
82		280	136	0.48	9.840	0.281	0.403	0.0112	0.177	0.004	-0.36	2418	19	2183	36	2625	5	0.90
80		46	34	0.74	6.460	0.176	0.364	0.0095	0.128	0.003	-0.06	2039	17	1998	29	2065	8	0.98
40		62	40	0.64	6.390	0.182	0.358	0.0097	0.130	0.003	-0.31	2030	18	1974	31	2095	9	0.97
37		151	53	0.35	6.426	0.151	0.358	0.0082	0.131	0.003	-0.19	2035	11	1972	19	2107	7	0.97
44		100	109	1.09	6.100	0.193	0.356	0.0108	0.124	0.003	-0.14	1989	21	1960	38	2020	8	0.99
2	Rim	444	141	0.32	8.210	0.198	0.355	0.0082	0.168	0.003	-0.31	2256	12	1958	19	2542	4	0.87
5		70	102	1.47	5.854	0.150	0.342	0.0090	0.125	0.003	0.01	1957	15	1895	28	2035	9	0.97
28		878	74	0.08	7.890	0.218	0.334	0.0090	0.173	0.004	-0.07	2218	18	1858	30	2584	10	0.84
48		28	15	0.53	6.030	0.251	0.334	0.0137	0.130	0.003	-0.12	1976	32	1856	58	2098	15	0.94
32		101	49	0.49	5.867	0.153	0.333	0.0085	0.129	0.003	0.18	1956	14	1853	26	2080	10	0.95
18		49	19	0.38	5.977	0.155	0.321	0.0083	0.137	0.003	0.03	1975	16	1799	23	2184	12	0.91
4		677	299	0.44	5.659	0.146	0.316	0.0080	0.130	0.003	-0.30	1924	14	1767	24	2103	5	0.92
83		48	22	0.47	5.510	0.163	0.314	0.0093	0.127	0.003	0.10	1906	20	1762	34	2056	15	0.93
39		125	113	0.90	5.190	0.144	0.309	0.0082	0.122	0.003	-0.39	1849	17	1737	27	1987	9	0.94
49		403	115	0.29	6.840	0.196	0.307	0.0083	0.161	0.003	-0.10	2090	18	1732	29	2466	9	0.83
35		182	124	0.68	5.660	0.158	0.298	0.0078	0.138	0.003	-0.22	1924	17	1683	25	2204	13	0.87
51		304	97	0.32	5.366	0.145	0.297	0.0079	0.131	0.003	-0.13	1878	16	1676	26	2111	5	0.89
66		693	223	0.32	6.470	0.176	0.295	0.0079	0.158	0.003	-0.11	2041	17	1664	26	2433	5	0.82
21		587	251	0.43	5.019	0.124	0.294	0.0070	0.125	0.003	-0.25	1824	12	1663	19	2028	5	0.91
16		118	107	0.91	5.043	0.126	0.294	0.0071	0.125	0.003	-0.23	1826	13	1660	20	2032	9	0.91
65		407	6	0.02	4.481	0.111	0.270	0.0067	0.120	0.002	0.15	1730	11	1539	20	1956	5	0.89
1		52	36	0.70	4.496	0.129	0.266	0.0072	0.122	0.003	-0.26	1729	17	1524	24	1995	14	0.88
22		128	32	0.25	4.144	0.103	0.266	0.0065	0.115	0.002	-0.13	1663	12	1519	19	1881	10	0.91
24		166	71	0.43	4.140	0.154	0.260	0.0086	0.117	0.002	-0.72	1660	25	1490	35	1910	12	0.90
54		66	43	0.64	4.218	0.118	0.253	0.0070	0.121	0.003	-0.09	1677	16	1452	25	1975	13	0.87
81		80	47	0.59	4.091	0.115	0.246	0.0068	0.120	0.003	0.00	1652	16	1417	24	1960	12	0.86
23		71	51	0.71	4.060	0.162	0.244	0.0080	0.121	0.003	-0.50	1650	29	1406	33	1979	15	0.85
31		41	17	0.41	3.840	0.134	0.236	0.0072	0.118	0.003	-0.29	1600	23	1367	28	1931	16	0.85
38		48	27	0.56	2.564	0.088	0.214	0.0072	0.087	0.002	0.00	1289	20	1251	31	1372	20	0.97
58		463	39	0.08	3.354	0.099	0.210	0.0060	0.116	0.002	-0.39	1496	18	1228	23	1903	10	0.82
46		275	126	0.46	2.377	0.068	0.208	0.0059	0.082	0.002	-0.19	1235	15	1219	22	1252	8	0.99
50		321	114	0.35	3.216	0.091	0.205	0.0059	0.115	0.002	-0.13	1463	16	1202	23	1876	8	0.82
9		53	45	0.84	2.485	0.076	0.170	0.0049	0.106	0.002	0.04	1267	17	1011	20	1724	17	0.80
41		36	16	0.45	2.302	0.077	0.156	0.0052	0.107	0.003	0.07	1211	19	935	23	1754	23	0.77
45		65	29	0.45	2.113	0.072	0.153	0.0047	0.100	0.002	-0.17	1152	19	919	20	1620	18	0.80
30		270	29	0.11	1.994	0.083	0.146	0.0049	0.099	0.002	-0.73	1111	25	878	22	1607	20	0.79
78		157	40	0.26	1.241	0.040	0.111	0.0031	0.081	0.002	-0.30	818	14	677	13	1215	19	0.83
77		397	18	0.05	1.284	0.042	0.111	0.0033	0.084	0.002	-0.40	838	15	675	14	1287	10	0.81
73		238	34	0.14	1.054	0.042	0.097	0.0028	0.077	0.002	-0.57	730	17	597	12	1121	24	0.82
19		224	185	0.83	0.775	0.020	0.096	0.0024	0.060	0.001	0.00	582	8	589	9	585	15	1.01
14		264	120	0.45	0.744	0.020	0.092	0.0024	0.059	0.001	0.06	564	8	567	10	564	18	1.00
69		39	33	0.84	0.687	0.022	0.089	0.0022	0.056	0.001	0.07	531	10	552	8	466	40	1.04
64		409	196	0.48	0.708	0.019	0.089	0.0021	0.058	0.001	0.02	544	8	549	7	531	15	1.01
56		37	66	1.77	0.693	0.026	0.089	0.0025	0.057	0.002	-0.24	534	13	548	10	494	49	1.02
52		113	49	0.44	0.720	0.022	0.088	0.0023	0.060	0.001	0.08	550	9	546	9	591	23	0.99
43		119	68	0.57	0.716	0.022	0.088	0.0025	0.059	0.001	-0.04	548	10	544	11	567	22	0.99
60	Core	148	95	0.64	0.708	0.019	0.087	0.0021	0.059	0.001	0.17	545	8	540	7	559	24	0.99
57		119	117	0.99	0.709	0.019	0.086	0.0024	0.059	0.001	0.20	544	7	532	10	574	24	0.98
62		456	176	0.39	0.691	0.018	0.086	0.0022	0.058	0.001	-0.01	535	8	532	8	539	12	1.00
27		61	45	0.74	0.681	0.023	0.086	0.0025	0.058	0.002	0.21	527	11	532	11	522	39	1.01
68		66	47	0.71	0.695	0.023	0.086	0.0023	0.058	0.001	0.04	535	11	531	9	558	33	0.99
42		136	114	0.84	0.692	0.020	0.086	0.0023	0.059	0.001	-0.12	534	9	530	9	551	24	0.99
13		184	64	0.35	0.674	0.017	0.085	0.0020	0.058	0.001	0.29	523	7	526	7	523	24	1.01
6		1215	931	0.77	0.694	0.016	0.085	0.0019	0.060	0.001	0.09	535	5	524	5	588	9	0.98
55		215	71	0.33	0.681	0.020	0.085	0.0021	0.058	0.001	-0.21	527	9	523	8	549	16	0.99
33		82	69	0.84	0.667	0.019	0.085	0.0025	0.058	0.001	0.10	519	9	523	10	512	26	1.01
12		74	55	0.75	0.656	0.018	0.084	0.0020	0.057	0.002	0.12	512	8	520	6	468	40	1.02
74	Core	48	38	0.78	0.675	0.021	0.084	0.0023	0.058	0.002	-0.04	524	10	519	9	520	42	0.99
34		296	229	0.77	0.655	0.017	0.083	0.0020	0.057	0.001	0.04	512	7	511	7	498	16	1.00
63		122	804	6.59	0.674	0.021	0.082	0.0022	0.059	0.001	-0.03	523	10	510	8	577	29	0.97
47		173	2	0.01	0.637	0.018	0.081	0.0019	0.058	0.001	-0.03	500	8	502	6	522	27	1.00
61	Rim	166	25	0.15	0.636	0.016	0.081	0.0020	0.057	0.001	0.25	500	6	502	7	481	18	1.00
7		763	40	0.05	0.761	0.021	0.080	0.0021	0.069	0.001	-0.49	575	8	497	8	903	13	0.86
67		394	4	0.01	0.635	0.015	0.079	0.0018	0.057	0.001	-0.15	499	5	493	6	500	14	0.99
75	Rim	222	5	0.02	0.625	0.017	0.079	0.0021	0.056	0.001	0.14	493	8	492	8	453	22	1.00
11		601	358	0.60	0.615	0.016	0.078	0.0020	0.057	0.001	0.02	487	6	486	7	501	13	1.00
26		125	103	0.82	0.604	0.015	0.078	0.0022	0.057	0.001	0.46	480	5	486	9	488	24	1.01
71		301	7	0.02	0.602	0.016	0.078	0.0020	0.056	0.001	0.18	478	6	482	7	453	19	1.01
29		261	11	0.04	0.685	0.082	0.077	0.0038	0.065	0.005	-0.90	524	46	479	21	740	140	0.90
10		393	91	0.23	0.582	0.016	0.075	0.0021	0.056	0.001	-0.13	465	7	468	8	463	14	1.00
53		253	8	0.03	0.581	0.017	0.075	0.0021	0.057	0.001	0.06	465	9	463	9	489	20	1.00
70		378	7	0.02	0.572	0.015	0.074	0.0019	0.055	0.001	0.11	459	7	458	8	434	17	1.00
17		337	12	0.03	0.535	0.013	0.072	0.0018	0.055	0.001	0.29	436	6	445	7	419	23	1.02
20		258	17	0.06	0.522	0.021	0.069	0.0027	0.055	0.001	-0.08	426	12	433	14	421	19	1.01
79		272	15	0.06	0.524	0.019	0.068	0.0023	0.056	0.001	-0.08	427	11	422	11	448	23	0.99
76		223	27	0.12	0.487	0.015	0.066	0.0018	0.054	0.001	-0.13	403	9	409	7	357	26	1.02
25		325	23	0.07	0.464	0.012	0.063	0.0016	0.053	0.001	0.10	387	5	396	6	352	14	1.02
59		989	54	0.05	0.474	0.012	0.062	0.0015	0.055	0.001	0.17	394	5	388	5	424	13	0.99
15		224	30	0.13	0.446	0.011	0.061	0.0014	0.053	0.001	0.06	375	5	380	4	337	22	1.01
36		1837	213	0.12	-0.001	0.000	0.000	0.0000	0.617	0.013	-0.46	-1	0	0	0	4547	6	0.08
8		937	352	0.38	-0.001	0.000	0.000	0.0000	0.576	0.012	-0.12	-1	0	0	0	4449	0	0.08

Table 4A_REE Zircon _McD_S sorted by age

Spot	Description	U (ppm)	Th (ppm)	Hf (ppm)	La (ppm)	Ce (ppm)	Pr (ppm)	Nd (ppm)	Sm (ppm)	Eu (ppm)	Gd (ppm)	Tb (ppm)	Dy (ppm)	Ho (ppm)	Er (ppm)	Tm (ppm)	Yb (ppm)	Lu (ppm)	Th/U	Yb/Gd	Eu/Eu*	Ce/Sm	Lu/Dy	U/Ce
8	c (h)	937	352	118738	0.13	29.04	3.49	9.41	45.27	22.38	337	609	1451	2381	3575	4818	5839	6870	0.38	29.63	0.18	2.66	0.47	53
36	c (h)	1837	213	191262	97.47	234.91	360.99	678.34	1304.05	710.48	980	590	691	934	1188	1866	2845	4106	0.12	0.61	0.63	0.75	0.59	13
15	r	224	30	113786	0.04	3.33	0.67	3.06	17.91	8.35	56	47	46	39	29	26	35	34	0.13	0.71	0.26	0.77	0.07	110
59	c (h)	989	54	115728	0.38	7.01	3.60	8.71	46.49	57.19	126	128	115	83	79	62	56	52	0.05	0.74	0.75	0.63	0.05	230
25	r	325	23	117864	0.04	2.64	0.48	1.38	11.35	7.99	32	36	46	60	84	155	213	309	0.07	4.06	0.42	0.96	0.67	200
76	r	223	27	121068	0.03	2.95	0.91	2.74	15.81	14.39	38	51	57	49	54	69	86	106	0.12	1.63	0.59	0.77	0.19	123
79	r	272	15	114466	0.05	0.86	0.68	1.88	7.84	6.04	40	142	277	330	292	231	177	170	0.06	2.89	0.34	0.46	0.06	514
20	r	258	17	118447	0.02	2.20	0.60	1.77	9.59	6.75	43	75	142	258	375	607	807	935	0.06	40.48	0.33	0.95	0.66	191
17	c (s)	337	12	126214	0.06	1.89	0.52	1.53	6.22	4.97	46	74	208	383	625	1263	1870	2439	0.03	29.29	0.29	1.26	1.17	291
70	r	378	7	126117	0.08	1.45	0.10	0.96	5.07	3.91	27	111	271	463	689	927	1093	1179	0.02	17.14	0.33	1.19	0.44	425
53	m	253	8	123981	0.09	1.22	0.18	0.59	4.19	3.55	35	99	235	372	541	644	652	626	0.03	13.00	0.29	1.21	0.27	338
10	c (h)	393	91	104563	0.03	57.59	0.64	2.12	9.05	6.75	66	122	283	504	813	1316	1764	2480	0.23	17.39	0.28	26.34	0.88	11
29	m	261	11	116505	0.05	3.13	0.27	0.81	3.38	3.20	32	72	179	295	488	785	1075	1488	0.04	40.00	0.31	3.84	0.83	136
71	r	301	7	123204	0.13	2.76	1.83	4.16	7.64	4.44	35	136	326	582	938	1433	1820	2276	0.02	27.14	0.27	1.50	0.70	178
26	c (s)	125	103	94660	0.13	21.86	2.38	5.86	41.08	29.66	146	227	393	625	901	1239	1553	1976	0.82	6.39	0.38	2.20	0.50	9
11	c (h)	601	358	131456	0.05	36.87	1.93	4.60	36.89	23.09	143	211	427	647	1019	1615	2373	3215	0.60	4.89	0.32	4.14	0.75	27
7	c (b)	763	40	131553	0.87	9.15	10.13	11.36	28.78	28.60	106	165	404	661	1075	1822	2658	3374	0.05	9.80	0.52	1.32	0.83	136
67	c (h)	394	4	122330	0.05	0.46	0.50	1.86	7.50	1.60	60	199	313	348	369	340	314	350	0.01	15.00	0.08	0.25	0.11	1407
75	c (o)	222	5	119417	0.26	1.11	1.01	1.77	7.09	4.44	48	157	299	366	412	413	360	423	0.02	7.65	0.24	0.65	0.14	326
47	m	173	2	120291	0.05	0.17	0.05	0.42	5.20	3.02	43	124	247	229	193	186	182	199	0.01	8.67	0.20	0.14	0.08	1619
61	c (h)	166	25	100291	0.05	12.07	0.44	1.31	10.07	7.46	46	106	241	366	534	806	1118	1398	0.15	5.52	0.35	4.97	0.58	22
63	c (h)	122	804	22524	0.74	64.11	20.58	62.36	185.81	467.14	553	861	1191	1363	1688	2126	2193	2309	6.59	1.11	1.46	1.43	0.19	3
34	o	296	229	109515	0.06	112.07	0.55	2.19	18.51	10.48	116	249	524	1007	1506	2324	2969	3943	0.77	24.81	0.23	25.07	0.75	4
74	m	48	38	92427	0.08	14.71	0.56	1.53	7.57	16.16	56	121	267	445	749	1255	1503	2114	0.78	9.09	0.79	8.05	0.79	5
12	o	74	55	84175	0.05	19.90	1.48	3.63	20.34	11.90	75	112	241	443	608	915	1286	1537	0.75	7.50	0.30	4.05	0.64	6
55	c (o)	215	71	99515	0.04	16.66	0.60	175.05	14.73	10.83	67	152	303	496	875	1215	1553	2130	0.33	12.92	0.34	4.68	0.70	21
6	c (o)	1215	931	83883	0.33	85.32	22.41	34.14	175.00	78.51	799	1127	2130	3205	4256	5980	7205	8699	0.77	12.47	0.21	2.02	0.41	23
33	o	82	69	77184	0.13	57.10	2.70	10.09	53.31	79.40	234	335	715	1081	1769	2725	3534	4634	0.84	7.16	0.71	4.44	0.65	2
13	c (o)	184	64	96602	0.01	14.68	0.51	1.20	11.08	8.88	72	122	262	467	719	1053	1360	1923	0.35	10.56	0.31	5.49	0.73	20
42	c (o)	136	114	70291	0.15	26.59	3.59	14.22	44.26	58.97	157	235	382	641	950	1547	2000	2642	0.84	6.67	0.71	2.49	0.69	8
68	c (o)	66	47	93981	0.07	23.00	0.38	2.41	8.65	11.55	39	97	172	262	478	652	842	1224	0.71	4.69	0.63	11.02	0.71	5
57	c (o)	119	117	74175	0.11	33.77	4.64	21.88	97.30	22.02	360	615	1085	1676	2350	2862	3385	3817	0.99	23.91	0.12	1.44	0.35	6
27	c (s)	61	45	90097	0.01	21.40	0.59	2.67	10.47	8.70	71	103	213	352	523	814	1056	1411	0.74	6.25	0.32	8.46	0.66	5
62	c (o)	456	176	98058	0.05	21.70	2.33	7.26	38.45	30.02	108	202	365	588	962	1421	2087	2907	0.39	4.62	0.47	2.34	0.80	34
60	m	148	95	93107	0.12	31.32	4.38	13.37	50.68	41.03	130	248	442	617	906	1360	1646	2150	0.64	6.22	0.51	2.56	0.49	8
43	c (o)	119	68	84466	0.05	11.00	0.75	3.94	22.77	27.18	77	152	326	496	773	1202	1559	2053	0.57	6.25	0.65	2.00	0.63	18
52	c (o)	113	49	110874	0.02	36.87	0.55	2.10	15.68	16.16	95	217	480	830	1400	2117	2944	4024	0.44	9.09	0.42	9.74	0.84	5
56	c (s)	37	66	90971	0.09	118.60	1.95	7.07	49.66	27.53	242	402	793	1201	1756	2275	2522	3256	1.77	13.41	0.25	9.89	0.41	1
64	c (o)	409	196	122136	0.05	45.35	0.86	3.41	20.27	1.78	101	224	480	835	1513	2275	2783	3638	0.48	30.00	0.04	9.27	0.76	15
69	c (h)	39	33	100583	0.01	19.90	0.66	1.82	12.16	14.03	57	121	226	374	623	834	1118	1553	0.84	5.25	0.53	6.78	0.69	3
14	c (h)	264	120	108835	0.01	27.08	1.31	2.47	11.35	3.91	72	116	253	449	688	1113	1404	1955	0.45	13.85	0.14	9.88	0.77	16
73	r	238	34	114369	0.09	10.28	1.86	4.97	21.62	15.81	75	189	289	447	575	810	901	1150	0.14	6.36	0.39	1.97	0.40	38

Table 4B_REE Zircon _McD_S sorted by age

Spot	Description	U (ppm)	Th (ppm)	Hf (ppm)	La (ppm)	Ce (ppm)	Pr (ppm)	Nd (ppm)	Sm (ppm)	Eu (ppm)	Gd (ppm)	Tb (ppm)	Dy (ppm)	Ho (ppm)	Er (ppm)	Tm (ppm)	Yb (ppm)	Lu (ppm)	Th/U	Yb/Gd	Eu/Eu*	Ce/Sm	Lu/Dy	U/Ce
19	o	224	185	100388	0.02	38.34	1.07	3.89	27.91	9.77	136	252	569	1004	1563	2413	3019	3813	0.83	34.50	0.16	5.69	0.67	10
77	m	397	18	123301	0.38	3.07	1.47	3.00	19.12	12.43	74	158	205	203	248	331	400	423	0.05	2.48	0.33	0.66	0.21	211
78	r	157	40	85631	0.18	11.75	1.50	1.95	6.01	11.19	28	53	89	121	238	416	573	907	0.26	3.62	0.86	8.09	1.02	22
30	r (o)	270	29	111068	0.04	4.26	0.24	0.94	6.15	6.22	55	120	256	410	628	955	1137	1402	0.11	13.53	0.34	2.87	0.55	103
45	c (s)	65	29	100971	0.05	7.94	0.17	1.05	9.32	8.35	26	66	132	194	333	474	609	793	0.45	6.19	0.54	3.53	0.60	13
41	c (h)	36	16	94660	0.03	15.01	0.44	1.55	7.09	9.77	47	71	138	225	406	619	814	1061	0.45	8.64	0.53	8.76	0.77	4
9	o	53	45	82718	0.03	35.73	1.76	4.99	21.35	13.68	101	129	269	434	559	789	1106	1358	0.84	7.62	0.30	6.93	0.50	2
50	c (o)	321	114	97087	0.38	18.76	0.80	3.74	14.46	18.29	59	108	226	379	621	976	1205	1565	0.35	8.21	0.62	5.37	0.69	28
58	c (o)	463	39	113010	0.30	4.32	1.37	2.47	15.54	14.92	59	124	200	273	375	502	632	850	0.08	2.94	0.49	1.15	0.43	175
46	c (h)	275	126	105825	0.03	41.60	0.69	3.44	25.34	3.37	137	260	488	766	1288	1753	2112	2817	0.46	23.13	0.06	6.80	0.58	11
38	c (o)	48	27	84078	0.05	13.51	1.23	4.46	22.50	9.59	107	174	341	549	869	1150	1547	2033	0.56	10.87	0.20	2.49	0.60	6
31	m	41	17	108350	0.04	15.50	0.22	0.83	6.08	4.97	13	29	51	104	181	307	492	720	0.41	6.40	0.57	10.56	1.40	4
22	c (h)	128	32	95728	0.01	1.75	0.68	2.52	9.59	1.15	26	23	54	61	102	136	167	199	0.25	8.14	0.07	0.75	0.37	119
24	c (h)	166	71	117573	0.02	6.04	1.00	3.04	17.91	4.97	86	94	126	132	143	153	151	157	0.43	2.56	0.13	1.40	0.12	45
65	c (s)	407	6	124078	0.02	0.44	0.29	0.88	13.58	2.13	89	216	261	218	201	213	239	239	0.02	3.55	0.06	0.13	0.09	1508
81	c (o)	80	47	79709	0.08	24.96	0.89	2.54	12.97	32.68	65	158	296	542	1025	1615	2348	3687	0.59	5.96	1.12	7.97	1.25	5
23	c (o)	71	51	90291	0.03	28.71	1.33	3.92	19.26	15.45	84	120	221	368	566	818	1236	1602	0.71	6.92	0.38	6.18	0.72	4
54	m	66	43	97379	0.31	22.51	0.82	3.79	16.28	10.48	76	125	205	344	533	794	981	1329	0.64	5.45	0.30	5.73	0.65	5
39	c (o)	125	113	92039	0.08	61.34	0.46	4.16	15.95	18.83	75	134	259	408	631	866	1261	1565	0.90	6.67	0.54	15.93	0.60	3
1	c (s)	52	36	89126	22.83	74.39	75.75	54.05	50.00	16.87	84	97	213	346	534	798	1186	1602	0.70	6.25	0.26	6.16	0.75	1
44	c (o)	100	109	83786	0.17	44.05	1.35	6.46	32.43	27.18	125	182	351	526	813	1097	1385	1772	1.09	5.43	0.43	5.63	0.50	4
21	o	587	251	110194	0.04	20.39	0.71	1.88	9.59	5.51	54	96	198	379	609	1000	1311	1748	0.43	10.40	0.24	8.80	0.88	47
16	c (o)	118	107	98835	8.02	83.20	86.21	78.77	76.35	27.89	118	124	251	425	650	1016	1478	2028	0.91	4.09	0.29	4.51	0.81	2
5	m	70	102	97767	0.01	25.61	0.58	1.33	5.81	4.80	36	60	136	222	373	595	786	1183	1.47	9.33	0.33	18.26	0.87	4
83	c (s)	48	22	81942	0.02	8.65	0.32	0.77	4.80	5.15	14	28	41	86	168	232	370	549	0.47	4.41	0.62	7.46	1.32	9
80	c (s)	46	34	98738	0.04	30.67	0.41	1.47	9.66	8.70	46	85	150	256	424	725	888	1240	0.74	7.08	0.41	13.15	0.83	2
32	o	101	49	103010	0.27	49.92	0.69	3.15	10.07	7.28	36	71	123	229	406	704	1075	1488	0.49	13.75	0.38	20.54	1.21	3
40	m (s)	62	40	89709	0.02	34.26	0.56	2.04	12.84	13.85	64	94	185	302	483	704	1025	1329	0.64	3.87	0.48	11.05	0.72	3
48	c (s)	28	15	91553	0.03	13.88	0.53	1.09	3.45	6.04	21	35	74	100	194	285	395	630	0.53	3.15	0.72	16.69	0.86	3
4	c (h)	677	299	110194	0.01	21.04	0.66	1.40	9.59	4.80	72	140	327	579	1025	1595	2329	3443	0.44	32.31	0.18	9.08	1.05	52
37	c (s)	151	53	94951	0.01	22.02	0.64	1.68	13.85	6.22	87	170	343	661	1150	1947	2391	3610	0.35	13.85	0.18	6.59	1.05	11
51	c (o)	304	97	107767	0.21	6.82	0.72	2.76	16.96	3.91	71	145	273	480	800	1089	1509	2167	0.32	17.65	0.11	1.67	0.79	73
18	c (o)	49	19	91553	0.05	10.77	0.73	1.01	9.12	5.51	42	80	186	344	500	846	1081	1439	0.38	17.33	0.28	4.89	0.77	7
35	o	182	124	99515	0.08	3.38	0.53	2.54	13.31	4.09	68	98	170	260	328	478	522	679	0.68	10.00	0.14	1.05	0.40	88
66	c (o)	693	223	106699	0.23	16.97	1.29	4.75	17.16	44.23	59	116	204	352	580	781	1081	1411	0.32	2.17	1.39	4.09	0.69	67
49	c (o)	403	115	125922	0.11	2.28	0.54	2.01	20.07	1.74	93	161	232	251	306	348	337	386	0.29	11.58	0.04	0.47	0.17	288
2	r	444	141	105728	0.09	8.40	1.38	2.54	15.68	7.82	90	129	267	425	611	899	1118	1610	0.32	8.18	0.21	2.22	0.60	86
28	c (h)	878	74	98350	0.48	11.97	4.04	6.48	16.82	8.88	35	61	97	171	259	445	646	878	0.08	7.78	0.37	2.95	0.90	120
72	r	495	22	110194	0.03	7.26	0.39	0.61	4.73	3.37	34	65	145	229	432	700	994	1504	0.04	16.92	0.27	6.36	1.04	111
82	c (b)	280	136	129029	0.07	3.34	0.82	3.22	22.16	2.49	76	151	215	242	269	308	269	250	0.48	9.17	0.06	0.63	0.12	137
3	c (h)	690	223	96505	0.10	12.72	2.78	7.72	48.58	15.28	233	280	577	837	1231	1846	2304	2959	0.32	10.91	0.14	1.08	0.51	88